UNIVERSITY
OF OSLO

Master's thesis

Photogrammetry of Unstable Rock Slopes

Deriving landslide motion of repeat airphotos with special attention to image distortions

Stewart George Robertson

Geomorphology and Geomatics

60 ECTS study points

Department of Geosciences

Faculty of Mathematics and Natural Sciences

Spring 2023

Stewart George Robertson

Photogrammetry of Unstable Rock Slopes

Deriving landslide motion of repeat airphotos with special attention to image distortions

Supervisor:

Andreas Max Kääb

Abstract

Providing temporal data of potential rock slope instabilities is important for assessing their dynamics and improving projections. Acquiring slope movement data prior to the advent of satellite radar can often only be found through the analysis of historical aerial photography. This project examines slope displacements over extended periods using photogrammetry techniques, improving orthorectified images with higher resolution digital elevation models (DEM) and comparing to orthoimages generated using lower-resolution DEMs. The orthoimages based on lower resolution DEMs are collected from Norge I Bilder (NIB), Norway's national archive of orthorectified images and readily available. The areas studied are Tussafoten and Skutshorn, with the present study showing that there has been movement dating back to 1969 and 1987 respectively. Raw aerial images are acquired and orthorectified through structure-from-motion for the Tussafoten slide, while NIB images are used for both Tussafoten and Skutshorn. By applying image matching to the different types of images, being single orthoimages, orthomosaic and NIB-images their displacement results are compared. Orthomosaics lead to a large range of displacements, including over stable ground, indicating uncertainty. The NIB-images use a coarse DEM with a 10 m resolution and have relatively large distortions in the steeper areas where the rockslides are occurring. Although the NIB-images are cheap and easily accessible, their distorted displacement values do suggest that they are not entirely correct. While the orthomosaics are mosaiced together from the single orthoimages, some of the distortion can be avoided by using the single orthoimages. The displacements from single orthoimages result in values that have a degree of certainty of 1 m, with results close to that which is expected from previous studies.

Acknowledgements

First, I would like to thank my supervisor Andreas Max Kääb who helped me form my thesis and put me on the right track. I appreciate the free reign for forming the thesis and working as I wished, something I have appreciated immensely.
Secondly, I would like to thank Trond Eiken for acquiring the images used for the thesis, and Luc Girod for help with processing said images in MicMac.

A thanks goes to "Russekontoret" and its students for keeping the study environment both social and professional. And to Jakob, for our discussions on all things geomatics and otherwise.

A huge thanks goes to the support of my parents, especially my father for proof-reading and attempting to correct my un-academic writing style. And a huge thanks to Edwin for making sure I was up every morning and for our enlightening twilight discussions.

Finally, thanks to Marlene for enduring me during this time.

Acronyms

2D/3D	2-/3-Dimensional
CP	Check point for accuracy of image
DEM	Digital Elevation Model
DSM	Digital Surface Model
DTM	Digital Terrain Model
GCP	Ground Control Point
GNSS	Global Navigation Satellite System
GSD	Ground Sampling Distance
InSAR	Interferometric Synthetic Aperture Radar
masl.	Meters above sea level
NGI	Geological Institute of Norway
NGU	Geological Survey of Norway
NIB	Norge i Bilder, national archive of orthorectified images, Kartverket
NVE	Norwegian Water Resources and Energy Directorate
NCC	Normalized cross-correlation
SIFT	Scale Invariant Feature Transform
SNR	Signal to noise ratio
SfM	Structure-from-Motion
TP	Tie Point
Φ	Correlation coefficient

Contents

List of Tables

List of Figures

Chapter 1

Introduction

Norway is a country famous for its fjords and valleys, with mountains rising sharply upwards from roads and villages. These structures make it susceptible to large rock mass failures, as population increases leads to land usage within hazardous areas (Pollock and Wartman 2020). The three most significant large rock mass failures in Norway occurred in the start of the 20^{th} century, two in Loen and one in Tafjord with a total loss of 186 lives. All three events resulted in rock masses falling into water, creating tidal waves. As long as man continues to inhabit areas in close proximity to potential failures, risk upon society will be present. Therefore, in order to minimise loss upon failure, mitigating risk as much as possible by implementing monitoring services which could help predict when potential failure might occur. Slow-moving landslides (mm $year^{-1}$ to 100 m $year^{-1}$) sometimes accelerate rapidly and fail catastrophically (Lacroix, Handwerger and Bièvre 2020). These slow moving motions have been found retrospectively and can be used as an identifier for rapid acceleration and failure (Carlà et al. 2019; Federico et al. 2012; Intrieri et al. 2018; Kilburn and Petley 2003).

Photogrammetry has been used for a relatively long time, this has often been in the form of aerial photography which is then used to create orthorectified photographs (Linder 2009). These are processed from the raw aerial image into a digital elevation model (DEM) which acts as the base for orthorectification. In addition to aerial images with known camera parameters, ground control points (GCPs) are required, which are objects that have a fixed geographic position. This study will both create orthorectified images from raw aerial images, and use images acquired readily made from Norge i bilder (NIB). NIB images cost less and are easy to acquire, they do face some limitations which will be

an important topic throughout this study.

Orthorectified images from different time periods are used to estimate the horizontal displacements in this study by using cross-correlation between the images, operated in the spatial domain (Kääb and Heid 2012; Kääb and Vollmer 2000). Through this we can get an estimate of displacements during the time lapsed between the two images. This method has been used to estimate velocities of earth mass movements (Debella-Gilo and Kääb 2011; Kääb, Girod and Berthling 2014; Scambos et al. 1992), among other methods (Lei, Gardner and Agram 2021; Messerli and Grinsted 2015; Nagy et al. 2019). The objects (in this case boulders or rock formations) need to be identifiable in both images, the area of interest needs to be free of variable vegetation (such as trees) and preferably not in north-facing slopes as they are prone to shadows.

This study will explore active known rock slopes under deformation that do not have temporal data prior to the active monitoring. The only way to expand the temporal data quantitatively (bar dating techniques) is through historical aerial photography. A challenging aspect with slopes is the difficulty in acquiring good quality imagery with GCPs as these areas are not interesting for most societal or economic purposes. They are in the most challenging topography possible, and there is often little to no interest for other subjects than safety in regards to these areas. In turn this means that there are relatively large distortions occurring in said photographs which need to be accounted for. The method used in this study has previously been utilized for active rock slope deformations (Kääb 2002). With the advent of InSAR being utilized across the entirety of Norway, many new instabilities are being identified and examined (Eian 2020). The ability to increase the temporal data available at a relatively low cost is thus an attractive option in the work of mitigating potential loss of economic values, and human lives.

1.1 Goal of thesis

The goal of this thesis is to find displacements of known active rockslides that are limited in spatial and temporal coverage. Analysis of repeat aerial photographs taken over a period of time are able to provide direct measurements of slope movements as long as there are images available. The goal is to obtain historical slope movements for comparison to modern ones. Areas of interest are challenging in that they have steep topography and issues with vegetation coverage effects.

Specific goals within the thesis are

1. Study effects of the orthorectification process and the resulting distortions
2. Determine the validity of measurements performed on images
3. Displacement average velocities of the active rock slope deformations Tussafoten and Skutshorn
4. If orthorectification of base imagery is necessary, or is data collected from Norge i Bilder satisfactory

1.2 Structure of the thesis

This thesis is divided into six chapters, these are split into sections which describe topics or subjects related to the respective chapter.

Chapter 2 describes the theory behind digital photogrammetry, image matching and InSAR.

Chapter 3 is a description of the study areas of Tussafoten and Skutshorn.

Chapter 4 presents the data and how it was used for DEM generation, orthorectification and image correlation.

Chapter 5 presents the results of the orthorectification, a comparison of distortions occurring between images and the resulting displacements from the rockslides.

Chapter 6 is a discussion of the results from the previous section, including interpretations and limitations.

Chapter 7 is a summary of the main findings of this study and recommendations for future work.

Chapter 2

Theory

To understand the processes and challenges of this study, some background in photogrammetry is necessary, how the image matching functions based on the orthorectified images. Therefore, the photogrammetry process will be presented before explaining the image matching.

2.1 Digital Photogrammetry

Photogrammetry is the science of measuring within photographic images to determine properties such as form, size and location. Image analysis is considered a part of photogrammetry. There are two photogrammetric products that are of particular relevance to this study, the DEM, and the orthoimage.

A (DEM) is a 3D-feature projected onto a 2D-surface. It is comprised of grids which indicate the georeferenced and associated height values in the center of each grid. The distance between two cells within the grid is noted as the resolution or Ground Sampling Distance (GSD).There are two main sub-categories of DEMs. A digital surface model (DSM) shows the terrain and all objects on it, such as trees and buildings and so forth (Rexer and Hirt 2014). The digital terrain model (DTM) is a product of the DSM where all objects are removed to solely represent the terrain (Kääb 2005). All DEMs created in this study will be in the form of DSMs.

Orthoimages are geometrically corrected and georeferenced images with primarily nadir viewpoint. These are created through a process called orthorectification, and requires a DEM and with a defined grid in terms of GSD. When using a DTM for this process, only

the ground would be orthorectified. To mitigate radial displacement, it is possible to use a DSM. This allows objects to be orthorectified and also leaves spots covered by said objects without data; such errors in the DEM would affect the accuracy of the orthoimage (Kääb 2005). "True" orthoimages allow for geometric correction, but have data voids if some areas are not photographed at least twice (Girod 2018). The projection error from the DEM would cause cells being projected incorrectly on the orthoimage, as illustrated in Figure 2.2.

2.1.1 DEM Generation and Orthoprojection

The concept starts by having two (or more) images (Im_1, Im_2), with information of the cameras internal characteristics (Image, location ($CameraPostion_{1/2}$ and orientation as shown in Figure 2.1. With this information it is possible to identify the same point (A) but in two different images from different angles ($a_{1/2}$). A 3D position is then computed by the intersection of projective rays from each image corresponding to the image of point A ($a_{1/2}$ - $CameraPosition_{1/2}$) (Girod 2018).

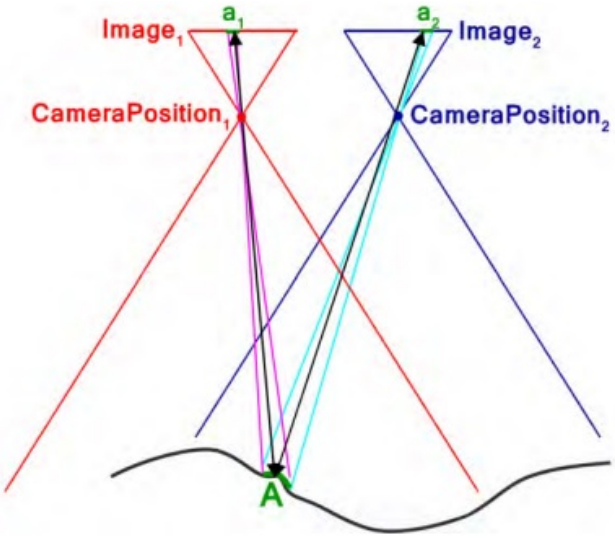

Figure 2.1: Concept of stereo-photogrammetry (Girod 2018).

The process of finding tie points (TP) is executed by using the Scale Invariant Feature Transform (SIFT) algorithm (Lowe 2004). SIFT identifies remarkable points that are brighter or darker than adjacent points that are given a description which is matched with points in another image (Girod 2022). These points are invariant to image scaling and rotation, and somewhat to varying illumination conditions and viewpoint (Lowe 2004; Westoby et al. 2012). The number of TPs is dependant on image sharpness, density and

resolution in relation to the texture of the area (Snavely 2008; Westoby et al. 2012). TPs are used to define an internal orientation of the relative camera positions. Combining the internal orientation with geolocation data allows one to calculate absolute camera positions. The geolocation data in this study is collected from Norge i Bilder (NIB) and input in the form of GCPs on the images. Geometrical correction is then performed using the GCPs to calculate a math model that warps the image to fit ground coordinates (PCIGeomatica 2019).

DEM Generation

Through dense correlation, the image correlation is used to compute the geometry of a scene (Furukawa and Ponce 2010). This results in a DSM, which is prone to some errors as seen in Figure 2.2.

The deviations of the DSM cause a horizontal shift of pixels within resulting images (Kääb and Vollmer 2000). According to Jensen (1996), accuracy of a DEM is a function of scale and resolution of the data, flying height, geometry of images, and stereoplotting instrument (photogrammetric software). Ackermann (1996) mentions how the accuracy of a smooth terrain is generally $^1/_{20}$th of linear grid size in accuracy, while rougher terrain is $^1/_{10}$th. Rough and steep terrain results in more spacing between DEM points in comparison to less steep and smoother (Manzer 1996). Generating the DSM also takes objects such as trees, boulders and other structures rising from the nominal terrain to be elevation at those points.

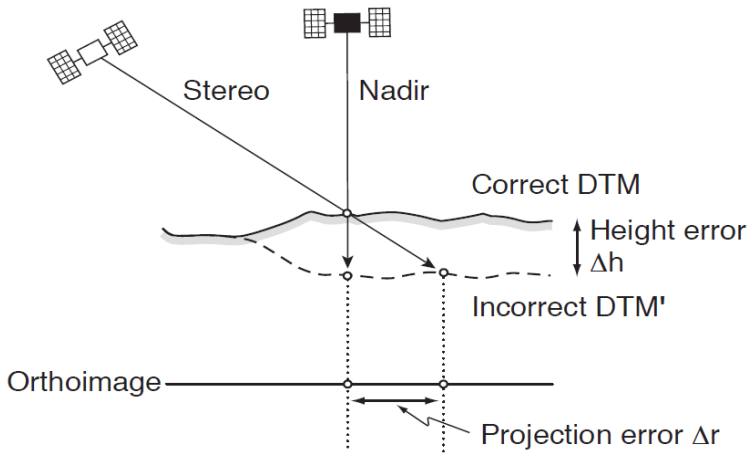

Figure 2.2: An incorrect DEM leads to horizontal projection errors in the orthoimage, the same principle applies to DSM as a DTM (Kääb 2005).

Orthoprojection

With the generated DSM it is possible to project the points in a 3D-space onto an image thus creating an orthoimage corrected for its terrain (PCIGeomatica 2019). Accuracy of a digital orthoimage is a function of the quality of imagery, GCP, photogrammetric triangulation and DEM (Jensen 1996). The absolute accuracy is largely based on the GCPs used in the DSM-generation (Manzer 1996). Some parts of the image may have stretch in it due to spike errors in the DSM, often more in steeper and or rougher areas.

Creating an orthomosaic is done by combining the existing orthoimages into one. The mosaicing process is performed by matching images by seam lines. The orthomosaic will be distorted in different directions based on the orthoimages incidence angle origin. This can create distortions in varying directions, based on where the images are connected. Two orthoimages of the same area (DEM) can be used to determine 3D coordinates (Baltsavias 1996). Furthermore, they should be very similar if from the same time period, except where there are radiometric differences and an incorrect DEM. The radiometric differences can according to Baltsavias (1996) be due to four factors; (1) differences in viewing angle, noise, illumnation, (2) occlusions, (3) inclined surfaces with different extent in the images or (4) shadows.

2.1.2 Camera lens and sensor parameters

Surface areas vary greatly in terms of reflectance. This can be due to time of day, shiny objects such as water which is always moving or from areas covered by shadows. Camera sensors are dependant on light reaching the sensor, but can also be negatively affected by direct sunlight which can create dark shadows on the surface. Parameters effecting the amount of light reaching the sensors include aperture, exposure time and sensitivity of the sensor. Where aperture influences the amount of travelling through the lens and sense of depth in addition to vignetting (Girod 2018), exposure time is how long the sensor is "active" and can receive light. Sensitivity or ISO numbers, is a standardized measure of the sensitivity of a sensor to light. Higher values of ISO increases brightness noise, and vice versa. Figure 2.3 shows how different exposure values can be interpreted where more "balanced" images are preferred. This study uses a normalized cross-correlation that takes care of these effects, though they could in principle have an effect on the final results.

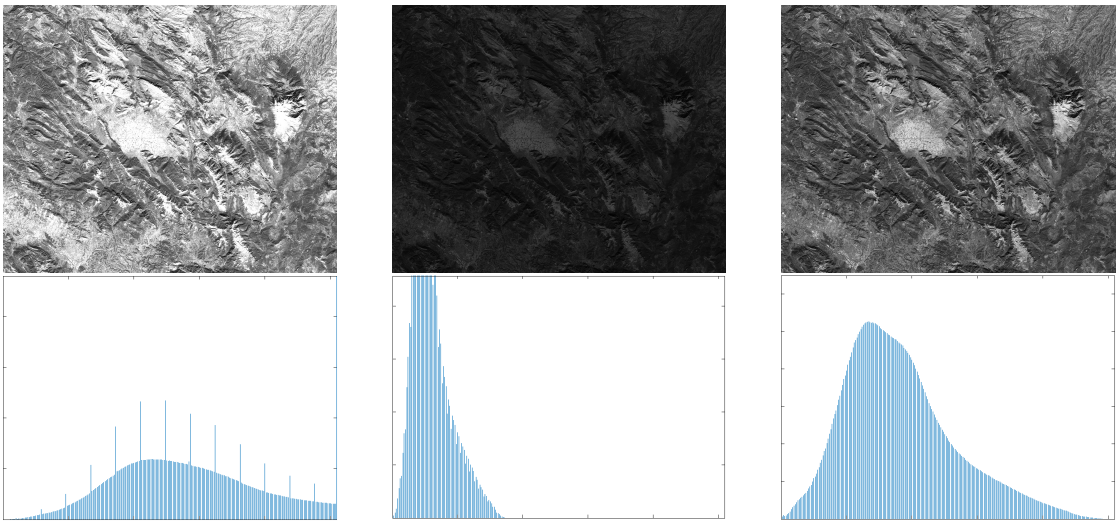

Figure 2.3: Scale of histogram (bottom) is black to white. Image enhancement/manipulation, the image on the left is overexposed and the image in the middle is underexposed. A balanced exposed image as seen on the right, where the grey values are mostly in the middle of the histogram (ESA and IGO 2022).

2.1.3 Optical Distortion

The images used in this study are taken with high-fidelity photogrammetric cameras and these effects are not a concern, it is however important to have a basic understanding. Distortions are the deviations of an ideal image taken from the theoretically perfect camera (Fig. 2.4). Geometric distortions happen due to the attempt of representing a 3D surface as a 2D image. This is further split into two categories, namely pincushion and barrel with mustache being a mixture of the distortions (Bernacki 2020). The barrel distortion decreases with distance from the optical axis, while pincushion is the opposite. Mustache (complex) has a barrel distortion close to the image centre, while becoming a pincushion near the edge.

Radiometric or chromatic distortions are the result of the variation of refractive index (Girod 2018). This can be caused by varying solar radiation conditions, scattering, sensor response and so forth (He, Liu and Shen 2019). These result in offset (η), scaling (λ) and random noise (e) (Debella-Gilo and Kääb 2012).

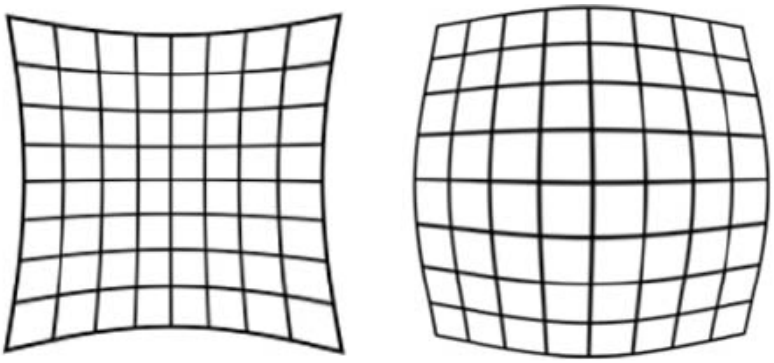

Figure 2.4: Radial geometric distortion of regular grids with a pincushion on the left and barrel on the right (Girod 2018)

2.2 Image matching and the CIAS software

Schenk (1999) describes three main matching techniques, namely feature-based, symbolic and area-based. Feature-based is a cost-function examination of the edges and regions to determine conjugate features. Symbolic matching is a cost-function that compares descriptions of images, for example gray-levels compared to the topological features. This study uses an area-based method which applies correlation of the gray levels. Thus the Correlation Image Analysis (CIAS) program is used to determine horizontal displacements of individual terrain features (Kääb and Heid 2012; Kääb and Vollmer 2000).

The input of two single-band grey scale orthophotos involves measuring displacement vectors by using *block matching*. Block matching compares image sections (grey values) to each other by a double cross-correlation function (Kääb and Vollmer 2000). This is done through two steps (Figure 2.5): a section of the image in time 1 is first chosen. This 'reference block' has its central pixel coordinate defined. Second, the corresponding image section ('test block') is searched for within an area ('test-area') of time 2. If found, a vector is established between the central pixel coordinates of time 1 and time 2, calculated through a normalized double cross-correlation (NCC) function based on grey values (Kääb and Vollmer 2000). The normalization allows for better comparison of grey-values with different illumination conditions and the correlation coefficient from different correlation tests can be compared (Kääb and Heid 2012). For finding the "correct" displacement vectors, two different methods within a threshold are commonly used: Either a threshold for a maximum correlation coefficient (Φ), or a threshold for the signal-to-noise ratio (SNR). SNR is the ratio between the maximum Φ and the average

Φ. Though other studies have used a threshold of Φ >= 0.6 or 0.8 to find the "correct" movements (Kääb and Vollmer 2000).

There are some limitations with the method of NCC (Debella-Gilo and Kääb 2011; Lewis 1995; Scambos et al. 1992; Schenk 1999). NCC is sensitive to noise, scale and rotation in the images. Important to regard that the displacement must be larger than the mean error of the image co-registration (Debella-Gilo and Kääb 2011).

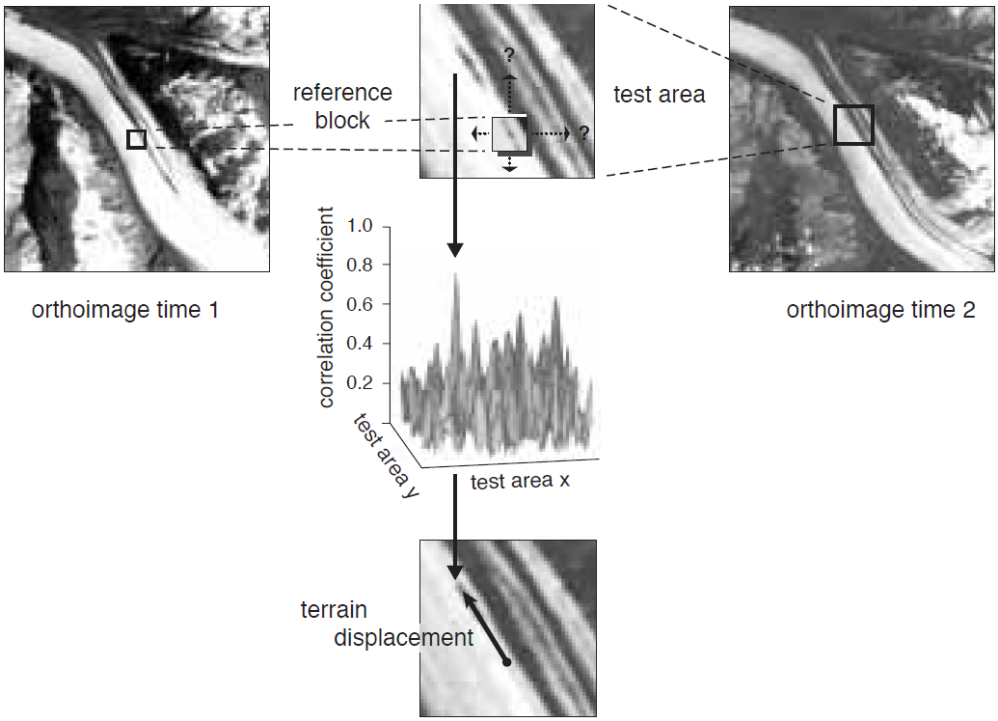

Figure 2.5: Principle of CIAS, reference block selected from first time step, test area from the second time step. The maximum correlation coefficient is then decided upon as the true displacement (Kääb and Heid 2012; Kääb and Vollmer 2000).

2.2.1 Similarity Transformation

A 2D-Helmert planar Transformation is possible using CIAS to co-register the images. This a similarity transformation that requires four parameters; scale (s_H), rotation (σ) and translations of x_{0H} and y_{0H} (Reit 2009). The equation 2.1 is used for the planar Helmert Transformation where **R** is a rotation matrix defined in equation 2.2. Here we can find rotation on the Z-axis, translation along X- and Y-axis in addition to scale changes (Watson 2006). TPs within it are required to find co-registration errors as these are the points used in the equations 2.1 and 2.2.

$$\begin{pmatrix} x \\ y \end{pmatrix} = \begin{pmatrix} x_{0H} \\ y_{0H} \end{pmatrix} + s_H \mathbf{R} \begin{pmatrix} x' \\ y' \end{pmatrix} \tag{2.1}$$

$$\mathbf{R} = \begin{pmatrix} cos\sigma & -sin\sigma \\ sin\sigma & cos\sigma \end{pmatrix} \tag{2.2}$$

2.3 InSAR

For comparison and explanation of how new slope displacements are currently (often) being discovered in Norway, radar interferometry is important. Interferometric Synthetic Aperture Radar (INSAR) is a useful tool for detecting and monitoring surface deformations. Openly available, INSAR Norge bases its displacement measurements on radar data from the EU's space program Copernicus (NGU 2022). These movements are defined by calculating the deformation-induced phase shift of back-scattered microwave signal between two coherent acquisitions of data points (Carlà et al. 2019). With a millimeter measurement accuracy and relatively high spatial resolution, this permits characterization of many active rockslide deformations as seen in Figure 2.6 (Lauknes et al. 2010). Displacements that are larger than the phase shift will not be correctly measured by InSAR as seen in Eriksen et al. (2018). Important to understand that InSAR does not function on snow and is updated once a year after the data from the spring/summer has been processed. InSAR in Norway has a temporal dataset going back to 2015, an important part of rockslide assessments is to have as large as possible temporal datasets to correctly determine when the slides velocity is increasing or decreasing. Regardless, InSAR is invaluable for slope failure detection and prediction (Wasowski and Bovenga 2014).

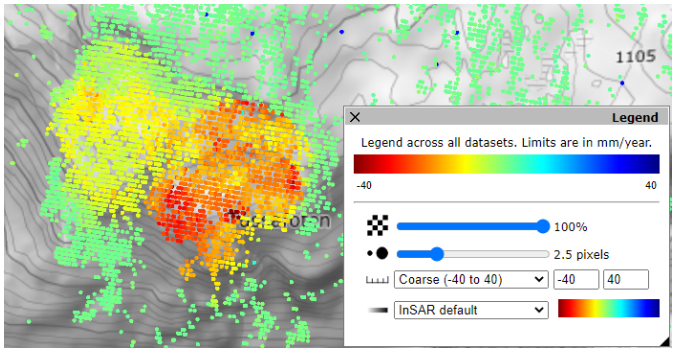

Figure 2.6: Snippet from InSAR-Norge of the Tussafoten displacement area.

Chapter 3

Study area

Two areas are selected for this thesis, Tussafoten and Skutshorn, they are investigated due to their active slow-moving deformation. Suitable aerial imagery going back further than 25 years was also a requirement for the choice of site. Additionally, they are south-facing slopes which largely avoid shadows and with little vegetation.

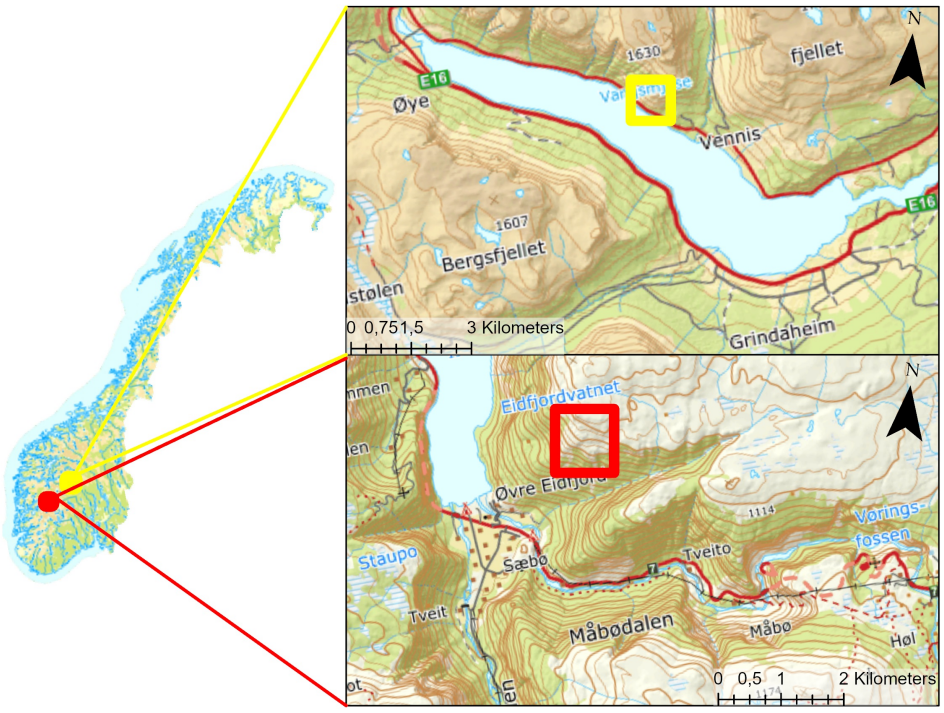

Figure 3.1: Tussafoten (red) and Skutshorn (yellow) on the Topografisk norgeskart 4 map from Kartverket.

3.1 Tussafoten

Tussafoten (Turtnalinuten 1171 masl.) is located above Øvre Eidfjord in Eidfjord municipality (60.436N, 7.155E). The slope itself is south facing with steep terrain partially extending down into Eidfjordvatnet and partially into the Juvedalen which terminates in Øvre Eidfjord. Figure 3.3 shows the potential areas that failures with varying return periods would affect (Glimsdal and Harbitz 2021). There are roughly 200 people residing in Øvre Eidfjord, and it is the final settlement before travelling over Hardangervidda. Additionally, it is commonly frequented by tourists to visit the Hardangervidda natural museum and the waterfall Vøringsfossen.

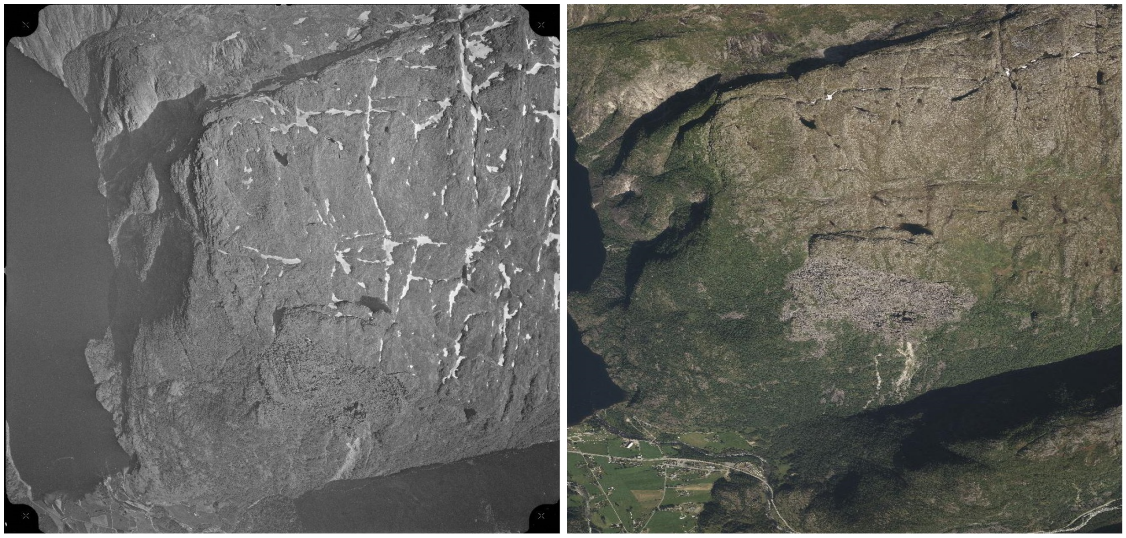

(a) 1969 (ot1a basis) (b) 2013 (ot2c basis)

Figure 3.2: Original aerial images used for orthorectification, the image from 2013 (b) is warped for presentation.

3.1.1 Previous studies and events

Tussafoten has been under investigation since 2016 and has had periods of differential GNSS measurements between 2018 and 2021 (Nicolet, Gunleiksrud et al. 2022). In situ measurements have been ongoing since 2021 to function as an early warning system (NVE 2022). Figure 3.3 shows possible failure paths and return periods which could damage infrastructure with potential for loss of life. The return periods are given in years and can potentially cause a floodwave which would affect a larger area of Øvre

Eidfjord than shown in Figure 3.3 (Glimsdal and Harbitz 2022). An estimated average of movement is at 1-4 cmyr^{-1} for the western part (A) and 4-10 cmyr^{-1} for the eastern part (B) (Nicolet and Böhme 2022). The eastern part of the slide is of main concern as there are no scenarios predicted where solely the western part reaches catastrophic failure (Nicolet and Böhme 2022).

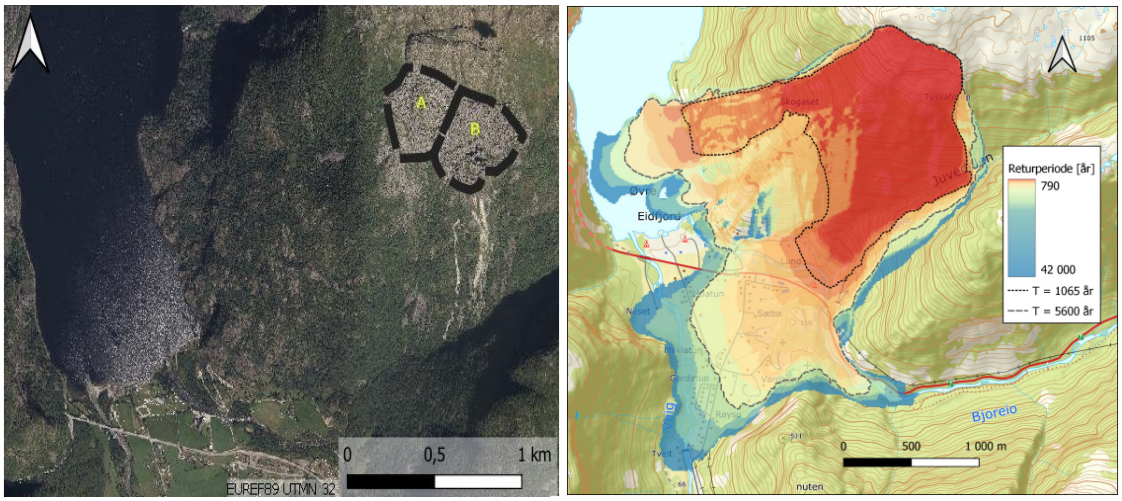

(a) Partial areas

(b) Return periods at failure

Figure 3.3: Sections of the Tussafoten slide on the NIB 2013 image (a), and possible failure path with return periods (b) from Glimsdal and Harbitz (2021).

3.2 Skutshorn

Skutshorn (1630 masl.) in Vang municipality, Norway (61.174N, 8.508E) has an instability that starts at roughly 1075 masl. above Kvitura. The south-facing steep terrain is positioned at the north-east shore of Vangsmjøse with a road in daily use below. Highway E16 travels along Vangsmjøse opposite to Skutshorn. E16 is the main road between western and eastern Norway, designed to be open during harsh winter conditions (Vogt and Nordrum 2017).

Figure 3.4: NIB image of the 2009 Skutshorn slide.

3.2.1 Previous studies and events

NVE decided in 2022 that within 2023 Skutshorn would be put under permanent surveillance based on investigations by NGU and NGI (Glimsdal and Harbitz 2022). Pullarello et al. (2021) also found through InSAR that the displacements have an average velocity of 2 cmyr^{-1} in the upper section and 0,5 cmyr^{-1} in the lower. There have been multiple incidences of rockfall in the area which caused the road to be closed for periods of time (Larsen 2020). A potential failure will cause a flood wave impacting the municipal centre of Grindaheim and the E16 highway through Vang (Glimsdal and Harbitz 2022). Figure 3.5 visualizes the return periods and damages that a failure at Skutshorn could initiate if a flood wave was created.

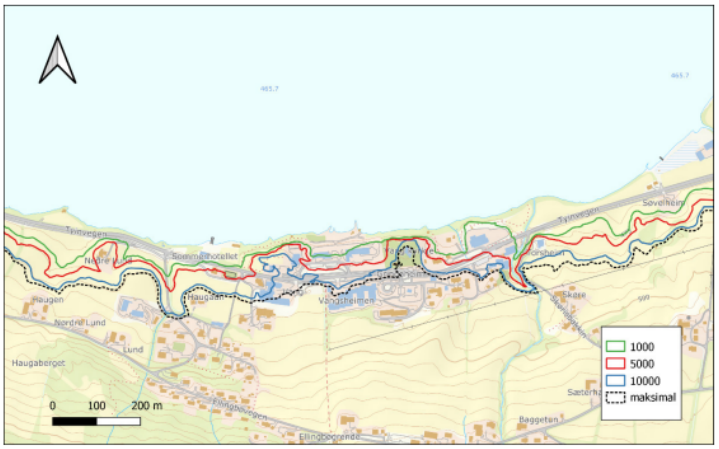

Figure 3.5: Grindaheim municipal center of Vang with tsunami return periods hazard zones (Glimsdal and Harbitz 2022).

Chapter 4

Data and methods

This chapter presents the data used and how it was analyzed, this process is represented in Figure 4.1. Orthomosaics of the study areas were acquired from NIB and original aerial imagery of Tussafoten from NGU through personal communication with Trond Eiken. Tussafoten orthomosaics from 1969, 2013 and 2019 from NIB were acquired in addition to the raw aerial imagery from 1969 and 2013. The raw aerial imagery required orthorectification before use, and all data was resampled to have an equal GSD. Similarly Skutshorn orthomosaics from 1982, 2009 and 2011 were acquired from NIB, but no raw aerial imagery.

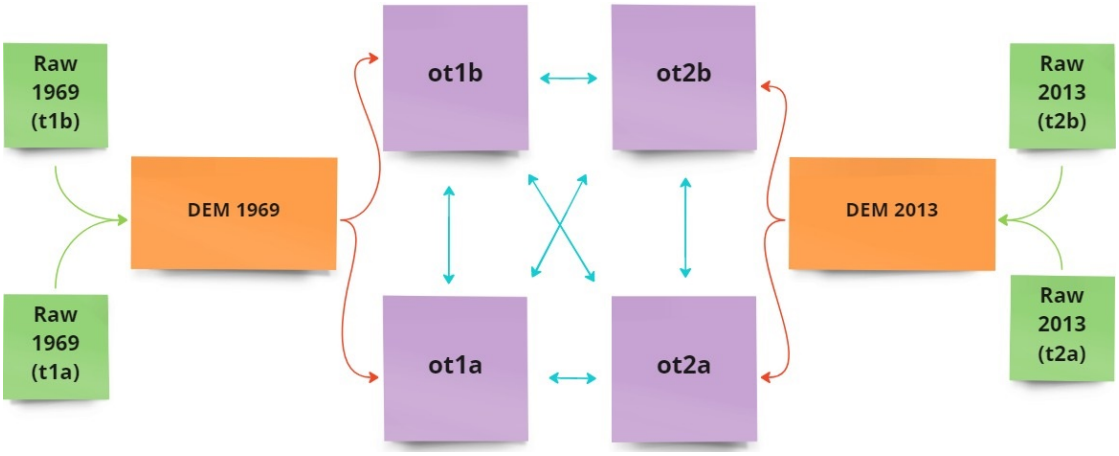

Figure 4.1: Distortion analysis workflow: Input images (green) used for DEM generation (green arrows) into a DEM (orange) which is then orthoprojected (red arrows) into orthoimages (purple). The orthoimages (Figure 4.4) are compared between each other (blue arrows) by using CIAS for image matching.

4.1 DEM Generation and Orthoprojection

Orthorectification was performed using the open-source photogrammetric suite MicMac. While an attempt was made to use Agisoft Metashape, the images from 1969 were lacking in quality. MicMac is a free open-source photogrammetric software created by the National Institute of Geographic and Forestry Information (IGN) and the National School of Geographic Sciences (ENSG) (Rupnik, Daakir and Pierrot Deseilligny 2017; Rupnik, Deseilligny et al. 2016). In contrast to many commercial software that have highly automated processes hidden within 'black-box' operations (Fraser 2013; Wackrow and Chandler 2011), MicMac allows for more customization within each process (Azarbayejani and Pentland 1995; Griffiths and Burningham 2019). The workflow for this study is based on the DEM Processing Using MicMac by McNabb (2022). The datasets from 1969 and 2013 of Tussafoten consisted of 3-4 images of the slide.

1. **Resampling images.** Performed on the images from 1969 as they had fiducial marks that required orientation of rays to object for a consistent geometry.

2. **Relative orientation.** Tapioca computes a sparse point cloud consisting of TPs by using the SIFT algorithm (Pierrot-Deseilligny 2022). For the images from 1969, a filter was created to avoid using the fiducial marks as TPs.

3. **Absolute orientation.** GCPs were collected from NIBs 2013 image of Tussafoten, which was created using a 10 metre DEM (Skistad 2014). These were then used to georeference the image as required for using CIAS.

4. **Dense point cloud.** Running a bundle adjustment results in a dense point cloud which refines the camera calibration further (McNabb 2022). The TPs and GCPs are used for resolving camera orientations while the camera calibration is also refined. The resulting point clouds are visualized in Figure 4.2.

5. **DSM and orthorectification.** The DSM is generated through the matching of ground geometry and ground-image geometry. During creation of the DSM, orthoimages are created from the raw images.

6. **Orthophotomosaic.** With the DSM it is possible to create the orthophotomosaic by mosaicing the orthorectified images from the previous step together.

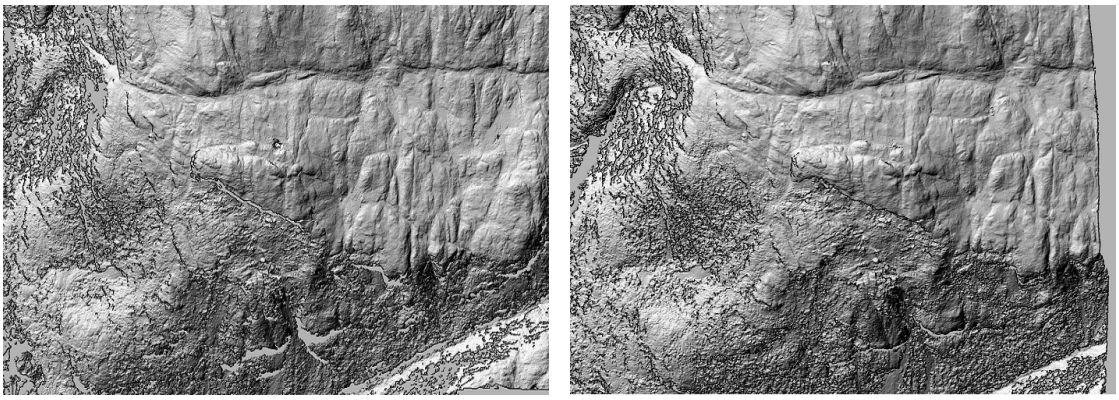

(a) DEM with hillshade from 1969

(b) DEM with hillshade from 2013

Figure 4.2: Generated DEMs from orthorectification processes, the noisy (rough) areas in the middle bottom indicate lack of coverage and in turn lack of elevation data in comparison to the smoother surface in the middle top.

4.1.1 Ground Control Points (GCP) and Checkpoints (CP)

The georeferencing is based on coordinates collected from NIB, and using images from 2013 as the basis, seen in Figure 4.3. Errors in the GCPs will lead to erroneously georeferenced DSMs and orthoimages. The accuracy of the coordinates from NIB were deemed to be have 5 metres uncertainty in world coordinates. During the processing these were additionally estimated to have a 2 pixel uncertainty (0.5 meters). The effect of random errors in GCPs are averaged out during the bundle adjustment, which decreases the error propagation from the NIB that was used to create aforementioned GCPs.

The CP validation is performed to show deviations of coordinates between the orthoimages. Chosen CPs are natural features visible in both years and assumed to be in a static position. Deviations are calculated by finding a North displacement (**dx**) and East displacement (**dy**). The 2D-distance ($\mathbf{2D}_{dist}$) is then found by using the Pythagorean theorem $2D_{dist} = \sqrt{(x_2 - x_1)^2 + (y_2 - y_1)^2}$.

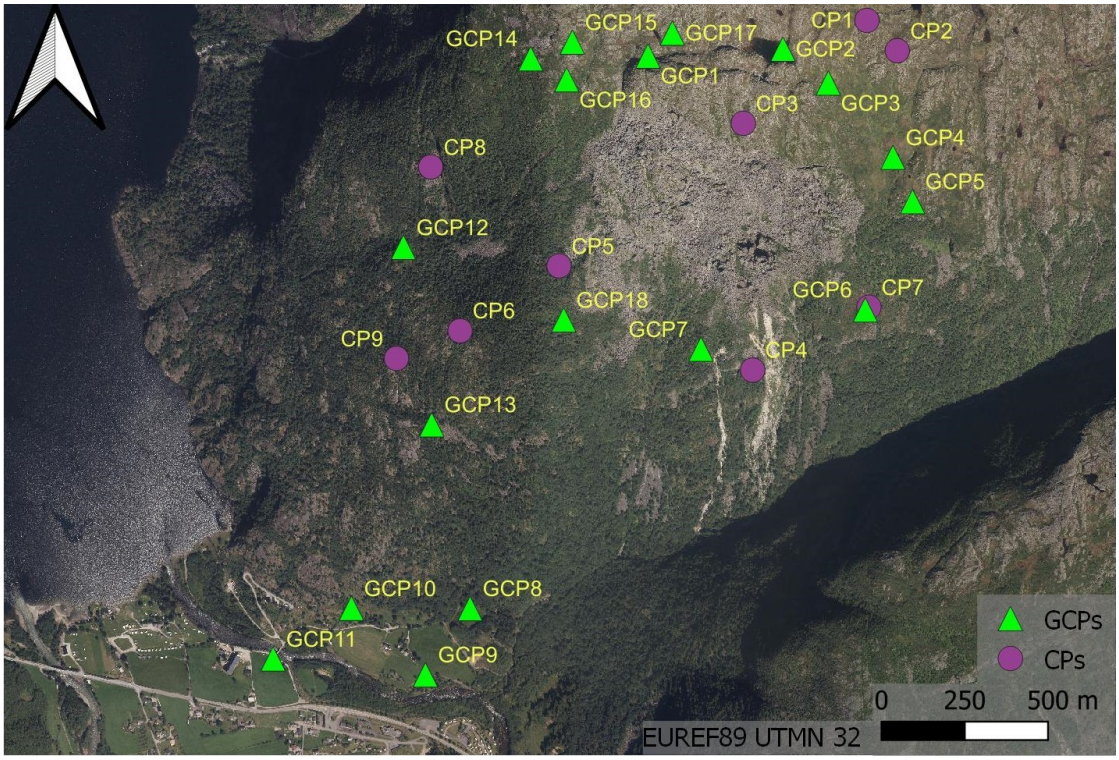

Figure 4.3: GCPs and CPs distributed across Tussafoten on the NIB-image from 2013.

4.2 Distortions

Presenting a 3D-structure on a 2D-plane inevitably causes some distortions (see section 2.1.1). Steep mountain rock slopes are among the most challenging topography, this creates distortions in the form of multiple areas not being visible from different scenes (behind ridges, rocks, slope angle). This results in both noise and error in the dense point cloud that further propagates into the generation of a DEM. NIB utilizes a national DTM when creating their orthomosaics, which has an accuracy of 10 m and is thus challenging to use in rough and steep areas. Through DEM-generation (section 4.1), a more accurate DSM is created. Also, in several of the NIB-orthomosaics there was insufficient coverage, which resulted in "holes" which were removed by editing the DTM to stretch over those "holes" (Finsrud 2017; Finsrud 2018). Editing a DEM further increases the deviations from the "true" position and or size.
This study opted for having no-data "holes" in the images used to calculate displacement as they would have less deviations from reality than if the DSM had been edited. Mosaicing orthoimages into an orthomosaic further increases distortions as it uses seam lines from the orthoimages that overlap. Additionally, the noise and errors from the DSM and the geometrical correction propagate into the orthomosaic.

4.2.1 Norge i bilder

The NIB-images follow the criteria and guidelines as set by Kartverket and Geovekst-forum (2020). Historical images do not have as strict criteria for their generation of orthomosaics that their more recent counterparts do. They can have artefacts due to physical altercations and systematic effects due to photography equipment, installation or other sources. Absolute accuracy requirements differ between areas and the area of interest falls under category D. Category D has the lowest economic value and is often defined as mountain areas. The requirements here are a standard deviation accuracy of 1.5 meters with a systematic deviation of 0.5 meters. Also, the requirements are not demanded where there are objects that are rising above the nominal terrain and cover an area of at least 1 square meter. Finally, areas with steep terrain where the DEM is lacking, the accuracy requirement can be disregarded.
The NIB-images of Tussafoten and Skutshorn from their first time period (1969, 1982 respectively) have had their DEMs edited (Finsrud 2017; Finsrud 2018). Both the 1969

and 1982 NIB-images were resampled to 0.25 meters as they were originally given with a GSD of 0.2 meters. The 2013 NIB-image which covers Tussafoten has errors specifically related the DTM in use (Skistad 2014), and has a GSD of 0.25 meters. The 2013 NIB-image of Skutshorn is described as following the criteria of "ortofoto 10" and is given with a GSD of 0.1 meters which was resampled for this study to a GSD of 0.25 meters.

4.3 Image correlation

Image correlation has been performed using CIAS for running numerous tests. Firstly, iterative testing was performed between each orthorectified image based on somewhat expected displacement velocities. Several different block sizes were examined with a test area of 100 pixels, the block sizes went from 15 to 50 at increments of 5 per sample, where a block size of 30 pixels was a good fit. The expected velocities are largely based on data from the InSAR Norway project which is managed by NGU, though some studies have examined these slides (Glimsdal and Harbitz 2022; Pullarello et al. 2021). Velocities largely determine the test area by using it as an average to find the expected displacement between the two time periods.

The image matching displacements over stable ground distortions are computed between each time period and orthoimage as seen in Figure 4.1 (blue lines). Distortions between the orthoimages (Fig. 4.4) are compared both visually and statistically. Orthoimages in this study are images that have been orthorectified, but have not been mosaiced together to create an orthomosaic of the images. The term orthomosaic for this study is the combination of the orthoimages combined together into a single image.
Visually, some areas are "stretched" or "blurred" due to conforming to the size and rotation from the viewing angle. The testing for distortions is run at a coarser scale than when looking for rock displacements, as this is an attempt to find a trend within the data. Statistics are split into two parts, stable ground statistics with "good" coverage and statistics from within the slide. The slide is located in a steeper part and has expected movements between each time period. Median values are selected over stable areas, to see the spread of distortions and attempt to account for systematic deviations.

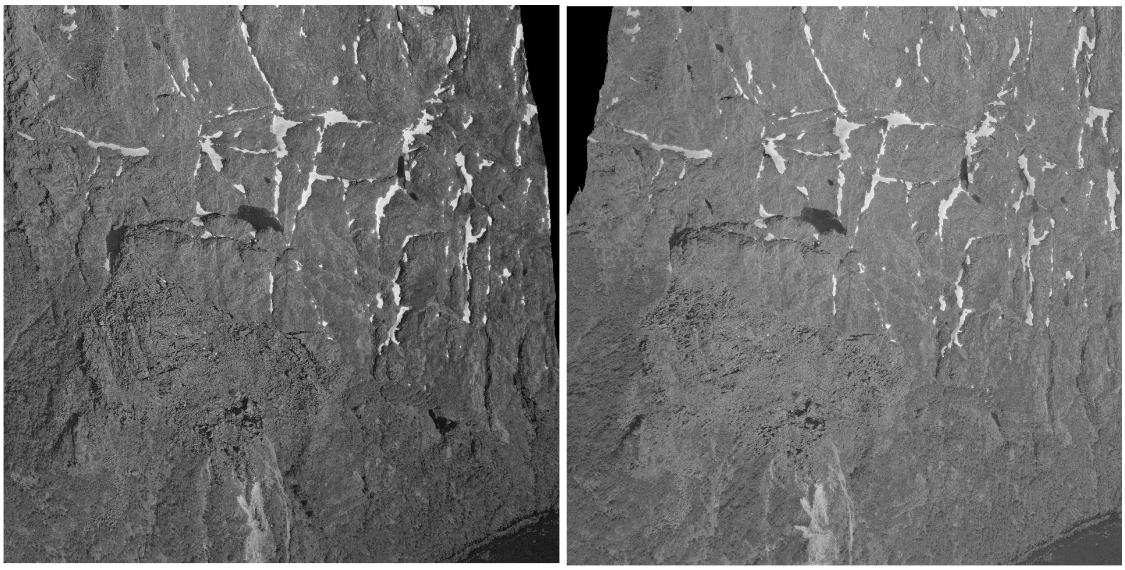

(a) 1969 ot1a

(b) 1969 ot1b

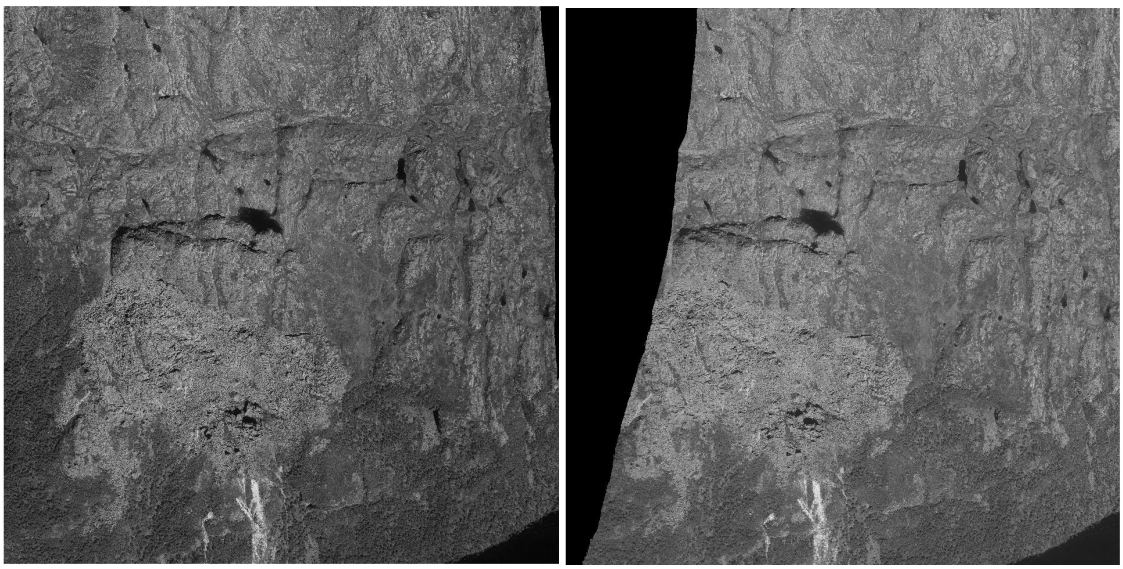

(c) 2013 ot2a

(d) 2013 ot2b

Figure 4.4: Single orthoimages of Tussafoten used for finding distortions and displacements as seen as purple boxes in Figure 4.1.

Chapter 5

Results

This chapter presents the results from methods described in Chapter 4. The orthorectification process is presented first as it forms the basis for the second and third steps: analysis of distortions between images (visually and related statistics) and the processing of displacement vectors.

5.1 Orthorectification

The images of *Tussafoten* in 1969 had too few tie points for the photogrammetric software Metashape by Agisoft to compute, there were no issues with computing the images from 2013. Consequently, only orthorectified images processed from MicMac are analysed here.

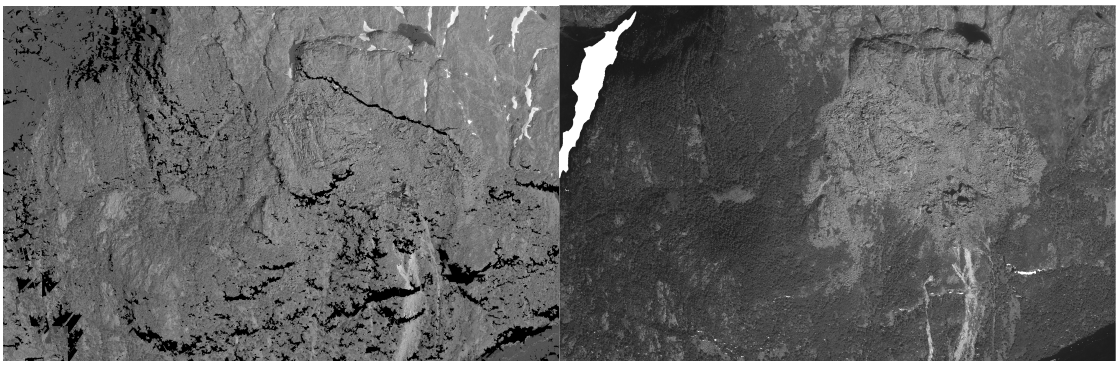

(a) Orthophotomosaic 1969 (b) Orthophotomosaic 2013

Figure 5.1: Orthomosaics of Tussafoten, null values is seen as black in (a) and white in (b).

TPs are the basis of matching images together and require remarkable points which must be clearly visible. The Tussafoten 1969 images, however, did have a significant amount of

issues when being mosaiced (Figure 5.2). The black areas in the 1969 orthoimages (white for the 2013 images), for example, do not have enough remarkable points to be defined, little contrast in the corresponding area in Figure 5.2(A, B) to the final product. There are several such areas within the orthophotomosaic from 1969 as seen in Figure 5.1(a). The white areas in Figure 5.1(b) is the same problem, visualized differently.

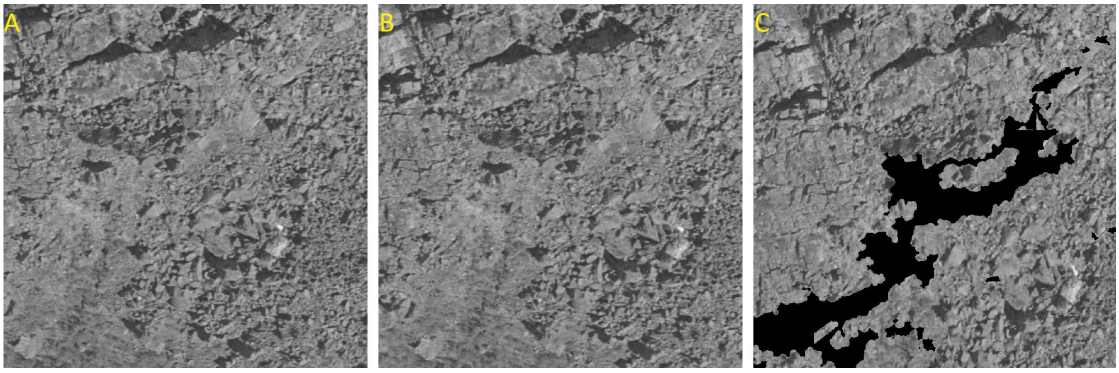

Figure 5.2: Tussafoten, images (A) and (B) are raw images that were the basis for (C) which is the 1969 orthomosaic with the black being null values.

In the Tussafoten 2013 images there is more contrast in comparison to the 1969 images (Figure 5.3). While the ridge itself is not very visible in either ot1a or ot1b of Figure 5.3, the shadow is the main indicator of the ridge's existence. Thus, images from 2013 show a more clearly defined ridge and consequently, result in an orthomosaic with less "holes". Section B (see Figure 3.3) of the Tussafoten slide is the area where the most suspected movement is located (Nicolet, Gunleiksrud et al. 2022). Figure 5.4 further shows how there is a difference in contrast and a stronger blurring effect in ot1a/ot1b compared to the ot2a/ot2b images.

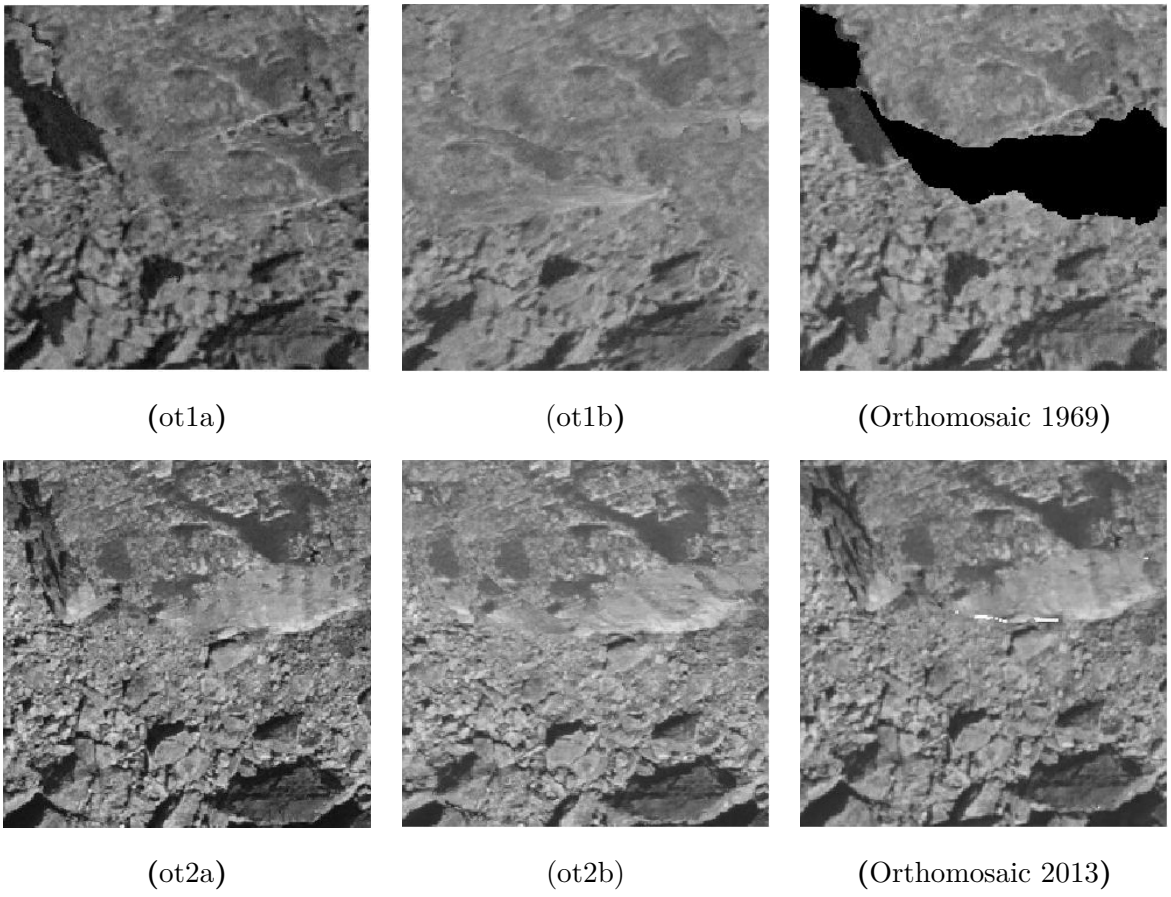

Figure 5.3: Backscarp of the Tussafoten slide, varying degrees of incidence angle, exposure and shadows effect on images. Image quality and overlap of objects show a strong effect as there is more contrast in the images from 2013 (ot2a/ot2b) compared to 1969 (ot1a/ot1b) resulting in somewhat lacking orthomosaic from 1969.

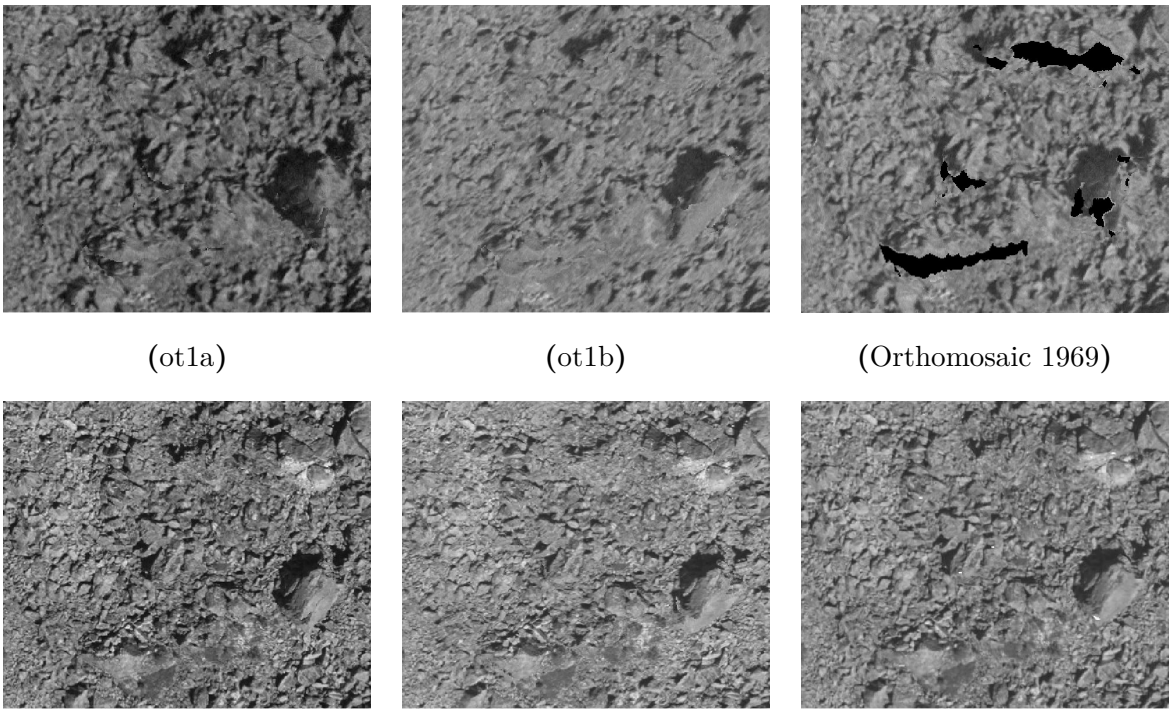

(ot1a) (ot1b) (Orthomosaic 1969)

(ot2a) (ot2b) (Orthomosaic 2013)

Figure 5.4: Close up images of section B from the Tussafoten slide. Image quality and overlap of objects show a strong effect as there is more contrast in the images from 2013 (ot2a/ot2b) compared to 1969 (ot1a/ot1b).

5.1.1 Accuracy

Checkpoints (CP) in Figure 4.3 are used to verify the accuracy of images. All checkpoints were used in the orthomosaic, some however do not appear in the orthoimages. The accuracy of the CPs in this case can be assumed to have a 1.5-meter uncertainty. Some of the points, in particular CP7 was difficult to define. An accuracy with a standard deviation for the **2d** being below the size of 4 pixels as seen in Table 5.1, Table 5.2 and Table 5.3. Checkpoints within an area that overlaps in all images were used and not discarded to give a clearer picture of deviations. Removing the "worst" checkpoints from the tables would lower their respective **M**-, and σ-values but would not be representative of the actual deviations within the image. Both the **M** and σ have a better quality than what would be expected through their NIB category D (Section 4.2.1). The Tables 5.1, 5.2 and 5.3 do indicate a positional accuracy predominantly between 0.5 to 1 meter in the orthoimages and orthomosaic.

Table 5.1: Checkpoint validation of orthoimages ot1a and ot1b with median (**M**) values and standard deviation (σ), all values are in meters.

ot1a				**ot1b**			
id	**dx**	**dy**	**2d**	**id**	**dx**	**dy**	**2d**
CP1	1,142	-0,106	1,036	CP1	1,123	-0,100	1,023
CP2	0,329	-0,012	0,318	CP2	0,481	0,183	0,664
CP3	0,086	0,422	0,508	CP3	0,076	0,412	0,489
CP4	2,068	-1,525	0,542	CP4	-1,077	-1,098	2,175
CP5	0,206	0,458	0,664	CP5	0,594	0,342	0,936
CP7	-0,980	-1,651	2,631	CP7	-0,592	-1,224	1,816
M	0,655	0,440	0,603	**M**	0,593	0,377	0,979
σ	0,688	0,652	0,783	σ	0,358	0,439	0,609

Table 5.2: CP validation of orthoimages **ot2a** and **ot2b** with median (**M**) values and standard deviation (σ), all values are in meters.

ot2a				**ot2b**			
id	**dx**	**dy**	**2d**	**id**	**dx**	**dy**	**2d**
CP1	0,900	0,094	0,994	CP1	0,847	0,154	1,001
CP2	0,229	0,231	0,460	CP2	0,393	0,424	0,817
CP3	0,105	0,393	0,498	CP3	0,097	0,353	0,449
CP4	0,088	0,289	0,377	CP4	-0,097	0,101	0,005
CP5	0,017	0,167	0,184	CP5	-0,003	-0,007	0,011
CP7	-1,058	-1,127	2,185	CP7	-1,177	-1,103	2,280
M	0,167	0,260	0,479	**M**	0,245	0,254	0,633
σ	0,417	0,345	0,673	σ	0,616	0,509	0,775

Table 5.3: CP validation of points from the orthomosaic of Tussafoten in 1969 and 2013 given in meters, where **M** is the median and σ is the standard deviation.

1969				2013			
id	**dx**	**dy**	**2d**	**id**	**dx**	**dy**	**2d**
CP1	1,104	0,045	1,105	CP1	0,714	0,321	0,783
CP2	0,755	-0,249	0,795	CP2	0,477	0,218	0,525
CP3	0,359	0,578	0,680	CP3	0,247	0,344	0,424
CP4	-0,091	0,047	0,102	CP4	-0,098	0,361	0,373
CP5	-0,041	-0,473	0,475	CP5	-0,074	0,010	0,075
CP6	0,310	-0,641	0,712	CP6	-1,520	-0,882	1,757
CP7	-1,672	2,503	3,010	CP7	-0,989	-0,252	1,021
CP8	-0,299	-0,168	0,343	CP8	-0,380	-0,217	0,437
M	0,135	-0,61	0,696	**M**	-0,086	-0,114	0,481
σ	0,781	0,935	0,845	σ	0,700	0,401	0,487

The co-registration parameters from a Helmert transformation result in deviations of their respective CPs. Table 5.4 shows that there is not much change in scale between the same time period, the rotation is as expected more pronounced than for the other values as the image was taken with a different incidence angle. The rotation to ot2a is larger than to ot2b, the shift is however substantially larger for both axis' to ot2b.
Table 5.5 gives very similar scale change to ot2b, and opposite to ot2a. Likewise for rotation, the change is greater to ot2a when compared to ot2b. The shift in **dx** and **dy** is larger than the pixel size. Less distortion in **scale** and **shift** to ot2a from both ot1a and ot2a when comparing to ot2b.

Table 5.4: Parameters for co-registration of orthoimages between ot1a and others found through the Helmert transformation.

	ot1a-ot1b		**ot1a-ot2a**		**ot1a-ot2b**	
Scale		0.9999		0.9982		1.0037
Rotation [deg]		-0.1016		-0.0768		-0.0469
Shift dx dy [m]	0.2083	-0.0729	-0.2292	0.6510	-2.0104	-1.4583

Table 5.5: Parameters for co-registration of orthoimages from ot1b to different time periods found through a Helmert transformation.

	ot1b-ot2a		**ot1b-ot2b**	
Scale		1.0023		1.0038
Rotation [deg]		-0.0480		0.0228
Shift dx dy [m]	-0.9374	-0.8072	-1.3698	1.4843

5.2 Comparison of distortions

The distortions shown are acquired from the middle part of Figure 4.1, where the purple images (Figure 4.4) are matched between each other (blue arrows). Distortions that occur between the images are defined by the color scale that ranges from lower sized distortions (green) through moderate (yellow) to large distortions (red) (Figure 5.5). Some of the images do not have overlap and are voided from the statistics, see Figure 4.4 or the red in the left-hand corner of Figure 5.5(c).

Center part of the images where there is most coverage naturally has the least amount of distortions and is mainly green in the center of the images. The slide is visible when comparing orthoimages between 1969 and 2013, but not in the same time period (Figure 5.5 (a), (d), (i), (l)). Either side of the slide is also facing different directions, with the western part facing South-West and the eastern part facing South, South-East. Different incidence angles to terrain that is not facing the camera, do result in larger distortions (yellow) the further off center (red) from where the image is.
The red line travelling from the top of the slide is a ridge which did not have enough coverage in 1969, but did in 2013 (Figure 5.5 (i, l) and Figure 5.3). Distortions above the slide are generally depressions which have some coverage issues. The lower part of the image is dominated by trees, vegetation and steep topography which resulted in a low amount of TPs. Less remarkable areas means less similar points which in turn results in random matching which is visualized as red.

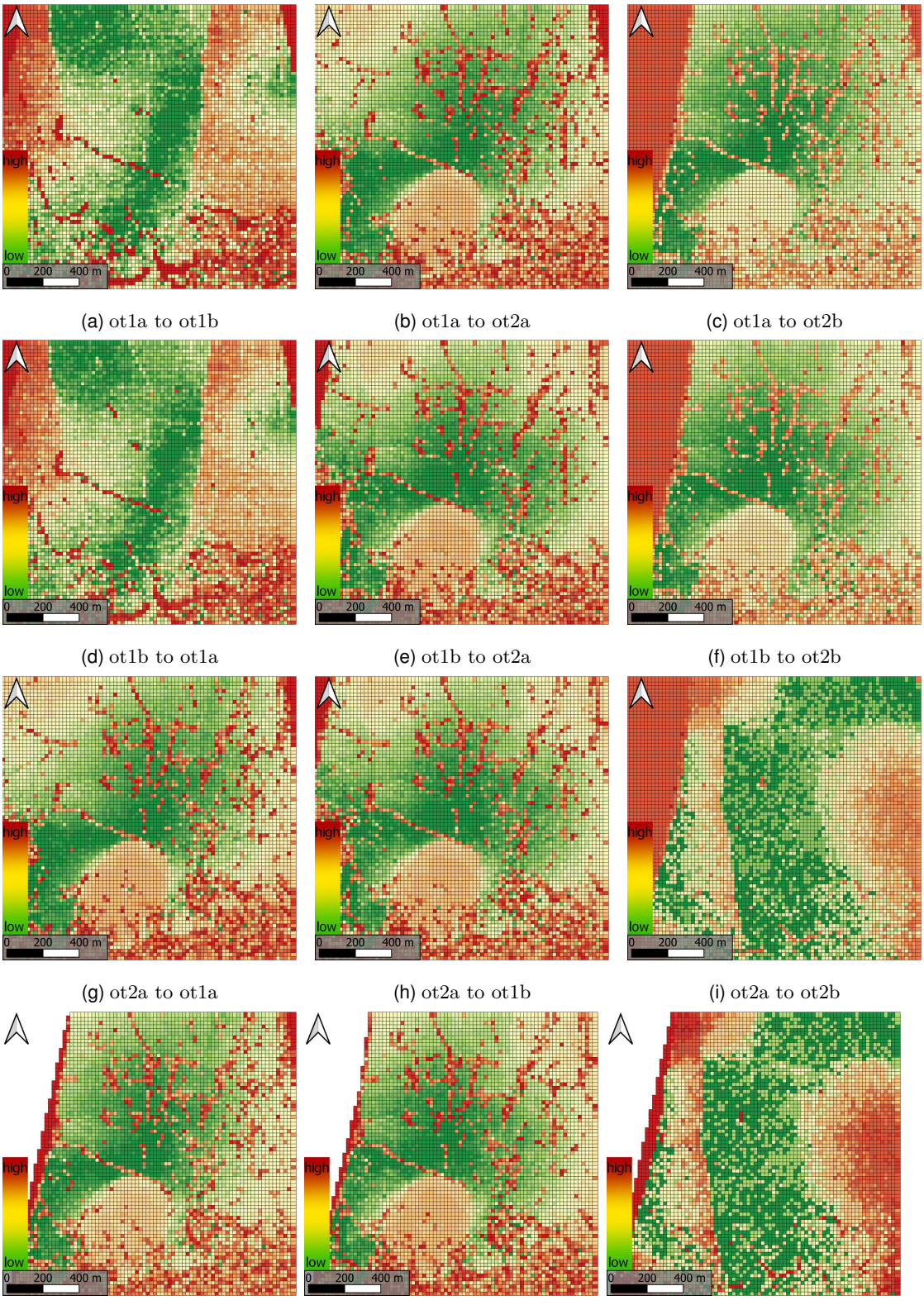

(a) ot1a to ot1b (b) ot1a to ot2a (c) ot1a to ot2b

(d) ot1b to ot1a (e) ot1b to ot2a (f) ot1b to ot2b

(g) ot2a to ot1a (h) ot2a to ot1b (i) ot2a to ot2b

(j) ot2b to ot1a (k) ot2b to ot1b (l) ot2b to ot2a

Figure 5.5: All combinations of orthoimages (Figure 4.4) distortions, with distortions ranging from low (green), moderate (yellow) to large (red). The slide is visible as an orange circular form in the bottom middle (between time periods) and the back scarp visible when comparing to orthoimages from 1969.

5.2.1 Distortion statistics

For considering the pairs that would be best matched together, a triangulation of vectors between the pairs has been calculated. Table 5.6 has several combinations of vectors that should in a perfect world result in 0 for the triangulation error. The median triangulation error is just above the size of 4 pixels. Distortions from ot1b are overall slightly smaller than from ot1a at a subpixel level.
The sum vector distortions along the x-, and y-axis should theoretically be equal to zero. Table 5.7 does show that most of the distortions are happening along the x-axis with **dx** being at the size of 3-4 pixels between the time periods. Sub-pixel to negligible distortions along the x-axis and sub-pixel distortion along the y-axis for the orthoimages does suggest that there is always distortion present, though the x-axis has the most issues.

Considering median-values within distortions on the stable ground, the values are lower than the pixel size for each time period as seen in Figure 5.6(a). There is a clear difference in distortions between the 1969 and 2013 orthoimages, where the 2013 images having significantly lower distortions between themselves. Figure 5.6 (b) and (c) results in a larger distortion between the images, with the deviation from the mean being larger when comparing distortions retrospectively. The median value is roughly 3 pixels for distortions between these time periods.

Table 5.6: Vectors from the distortion statistics over Tussafoten stable ground are used for calculating triangulation errors between three connected pairs that ideally should equal to zero. The errors are given in meters where the length is a 2D-distance

Combination	**Triangulation error**
ot1a-ot2a + ot2a-ot2b = ot1a-ot2b	1.07
ot1b-ot2b + ot2b-ot2a = ot1b-ot2a	1.13
ot1b-ot2a + ot2a-ot2b = ot1b-ot2b	1.06
ot1b-ot2b + ot2b-ot2a = ot1b-ot2a	1.01

Table 5.7: Median values from stable ground between orthoimages of Tussafoten given in meters. The **dx** represents the distortion along the x-axis, while **dy** is the distortion along the y-axis.

Between	**dx**	**Between**	**dy**
ot1a to ot1b	0	ot1a to ot1b	0.0312
ot1a to ot2a	0.5937	ot1a to ot2a	0.0312
ot1a to ot2b	0.5312	ot1a to ot2b	0.0625
ot1b to ot2a	0.5625	ot1b to ot2a	0.125
ot1b to ot2b	0.5	ot1b to ot2b	-0.1875
ot2a to ot2b	-0.0312	ot2a to ot2b	-0.0312

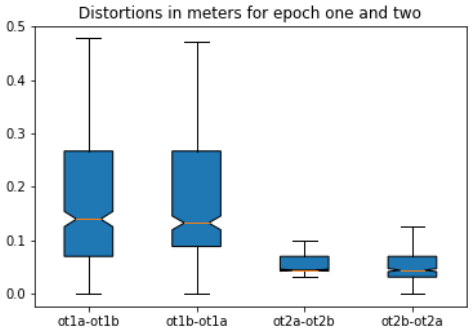

(a)

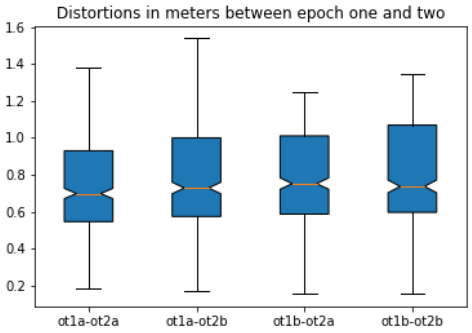

(b)

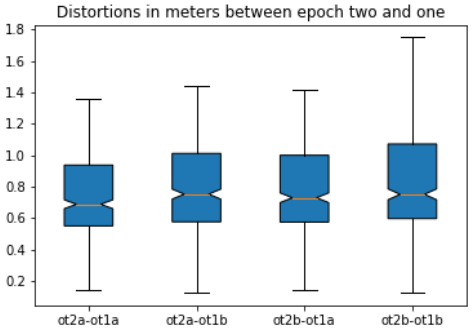

(c)

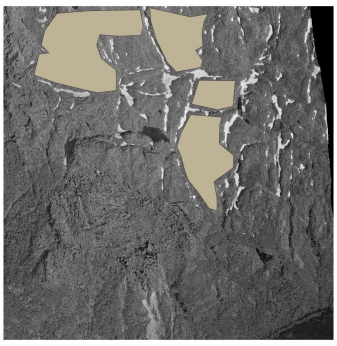

(d)

Figure 5.6: Boxplots based on the orthorectified images before mosaicing the polygons as seen in (d), these are chosen as stable ground which should be identical in each time period. Some images do not have data in their entirety and are not covered by polygons (Figure 4.4).

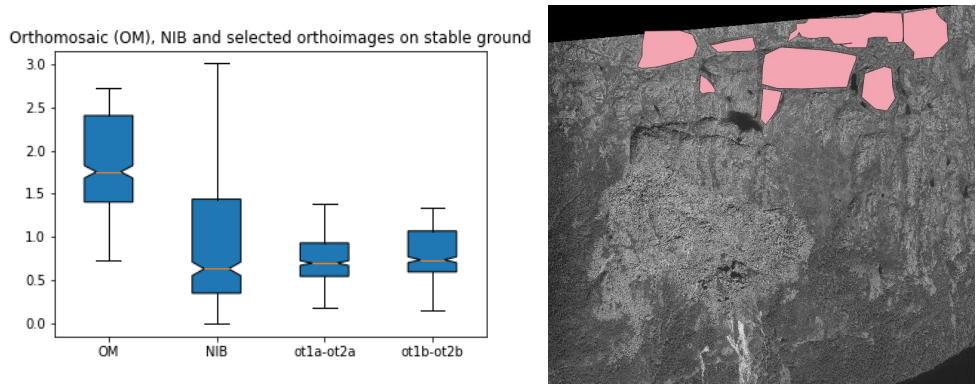

(a) (b)

Figure 5.7: Orthomosaic (OM) and NIB distortions between images of Tussafoten from 1969 and 2013 over stable ground in addition to orthoimage stats (a) from the stable ground as seen in (b)

5.3 Displacements

Suspected displacement vectors between time periods for both Tussafoten and Skutshorn. Tussafoten has displacement vectors from the orthoimages, the orthomosaic and the NIB-images presented in said order. Skutshorn solely relies on the images from NIB and is presented at the end of the chapter.

5.3.1 Tussafoten

The average displacement from InSAR Norge between 2015-2022 is at 0,8 cmyr^{-1} for section A and 1,9 cmyr^{-1} for section B. An averaged displacement after 43 years would be 36 cm (A) or 85 cm (B) based on the aforementioned values. Nicolet and Böhme (2022) have found the displacement velocity of section A to be at 1-4 cmyr^{-1} and section B to be between 4-10 cmyr^{-1}.

Section A orthoimage displacements result (Table 5.8) in a median displacement of between 0,24-0,36 meters (0,6-0,8 cmyr^{-1}) and a mean of between 0,30-0,42 (0,7-0,9 cmyr^{-1}) which is similar to InSAR displacement velocities. Maximum values seen in Table 5.8 have a larger spread when comparing to other values within the displacement, ranging from 1,25-2,13 meters (2,9-4,9 cmyr^{-1}). Both maximum displacements that exceed the findings of Nicolet and Böhme (2022) are found in displacement between ot1a/b and ot2a, while ot2b has a lower maximum for both orthoimages.
The orthomosaic displacements (OM6913) indicates median and mean displacements

several times larger than the orthoimages. While the displacements presented are larger, the spread of measurements are not much different from the orthoimages. The NIB displacements (NIB6913) is very similar to the OM6913 lengths when comparing the mean, otherwise it has a significant spread of values. With a maximum displacement of 11,89 meters (27,6 cmyr^{-1}) and a spread of 1,4 meters in the IQR with a σ of 1,13 does indicate accuracy and precision issues.

Table 5.8: Statistics of section A given in meters with **M** being the median and σ being the standard deviation, cmyr^{-1} is from the **M** after being averaged out over the 43 years between.

Images	**M**	**Mean**	**Max**	**Q1**	**Q3**	**IQR**	σ	cmyr^{-1}
ot1a ot2a	0,24	0,30	1,94	0,14	0,37	0,23	0,24	0,5
ot1a ot2b	0,32	0,38	1,25	0,22	0,47	0,25	0,25	0,7
ot1b ot2a	0,33	0,40	2,13	0,18	0,51	0,32	0,31	0,7
ot1b ot2b	0,36	0,42	1,60	0,22	0,55	0,33	0,28	0,8
OM6913	1,39	1,46	2,52	1,23	1,67	0,43	0,31	3,2
NIB6913	0,88	1,46	11,89	0,49	1,88	1,40	1,13	2,0

Section B of the orthoimage displacement result (Table 5.9) in a median between 2,27-2,36 meters and 2,06-2,18 meters for the mean. These findings are similar to Nicolet and Böhme (2022)(Section 3.1.1), the InSAR values do not result in such large displacements by design. The max displacement varies between 2,7-3,3 m (6,3-7,6 cmyr^{-1}) and is also within the range of previous studies.

Similarly to section A, NIB6913 of section B has a max displacement significantly larger than other displacement results. The same trend follows for the rest of the statistics, while not as large a difference, the range is still significant. OM6913 has values for the mean and median that are lower than that found in the orthoimages. There are larger ranges within the statistics of OM6913 and NIB6913 which make defining the true displacement ambiguous.

Table 5.9: Description of section B given in meters with **M** being the median and σ being the standard deviation, cmyr^{-1} is from **M** after being averaged out over the 43 years between.

Images	**M**	**Mean**	**Max**	**Q1**	**Q3**	**IQR**	σ	cmyr^{-1}
ot1a ot2a	2,27	2,09	3,08	1,85	2,47	0,62	0,54	5,3
ot1a ot2b	2,29	2,06	2,73	1,79	2,49	0,69	0,59	5,3
ot1b ot2a	2,31	2,13	3,04	1,85	2,47	0,63	0,52	5,4
ot1b ot2b	2,36	2,18	3,28	1,91	2,52	0,61	0,52	5,5
OM6913	1,81	1,65	3,09	1,15	2,10	0,96	0,64	4,2
NIB6913	3,77	3,96	11,15	3,03	4,63	1,60	1,59	8,8

Orthoimages

Figure 5.8**(a)** shows displacement vectors of up to 0.5 meters with increasing lengths towards section B. Section B has for both **(a)** and **(b)** larger displacement vectors, mainly ranging from 2 - 3 meters in length. Comparing Figure 5.8 **(a)** and **(b)** can indicate that the incidence angle between ot1a-ot2a is more similar than ot1a-ot2b. Finally the arrows in the upper left of both **(a)** and **(b)** indicate movement travelling up-slope.
Figure 5.9 **(a)** and **(b)** are very similar in their displacement values. Section A has been displaced between 0.5 and 1 meters. Section B is moving with a displacement of between 2 - 3 meters in length. Similarly to Figure 5.8, both **(a)** and **(b)** of Figure 5.9 indicate movement travelling up slope in the upper left corner.

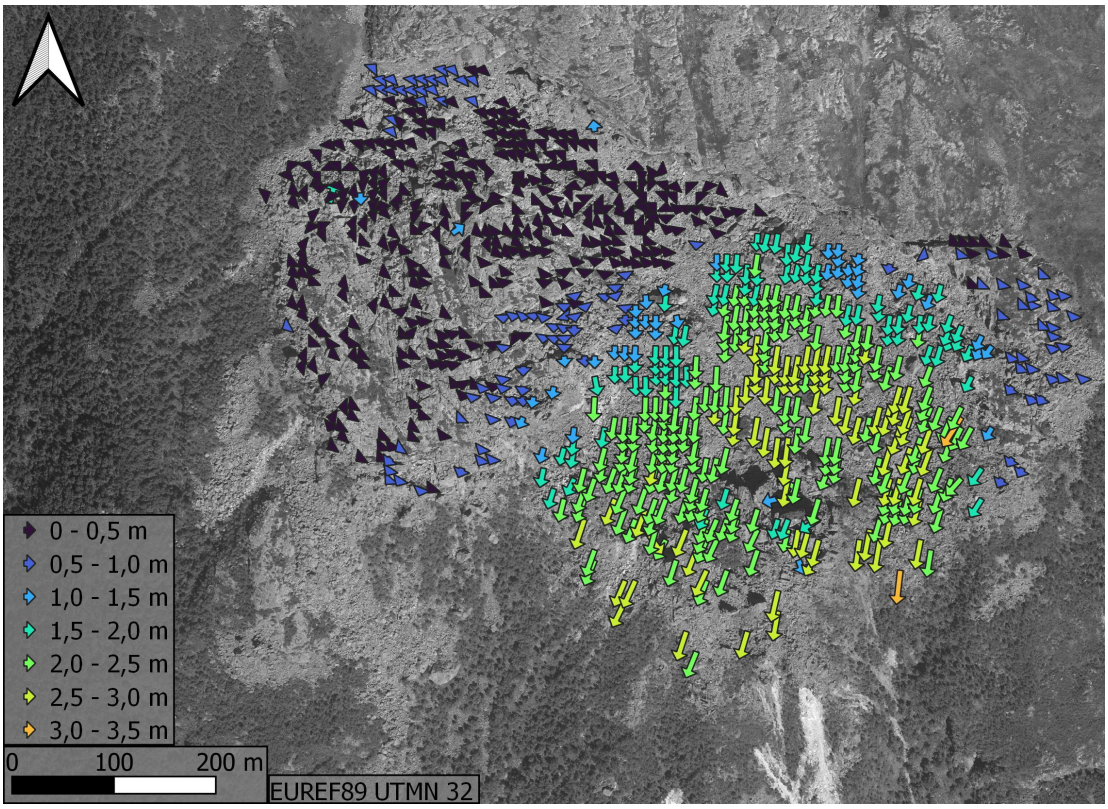

(a) ot1a to ot2a

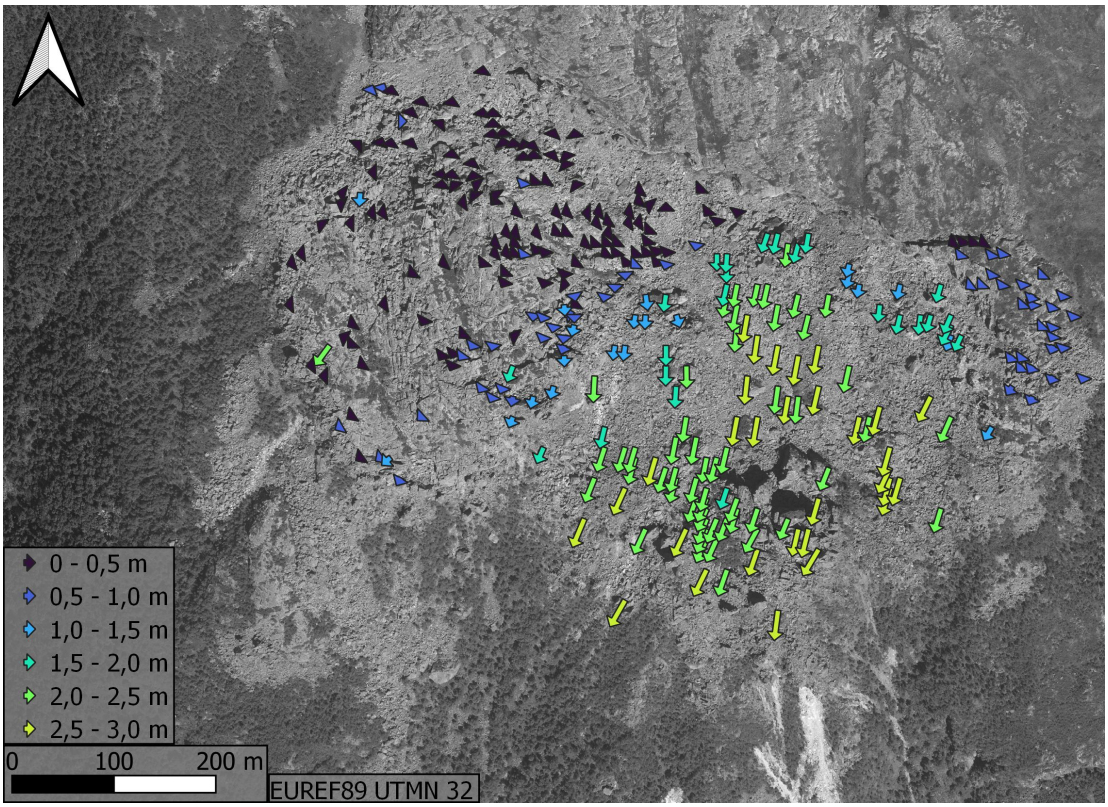

(b) ot1a to ot2b

Figure 5.8: Image matching of ot1a to both ot2a and ot2b, where measurements with $\Phi > 0.7$ are filtered out, resulting in 30% visible in **(a)** and 11% in **(b)**.

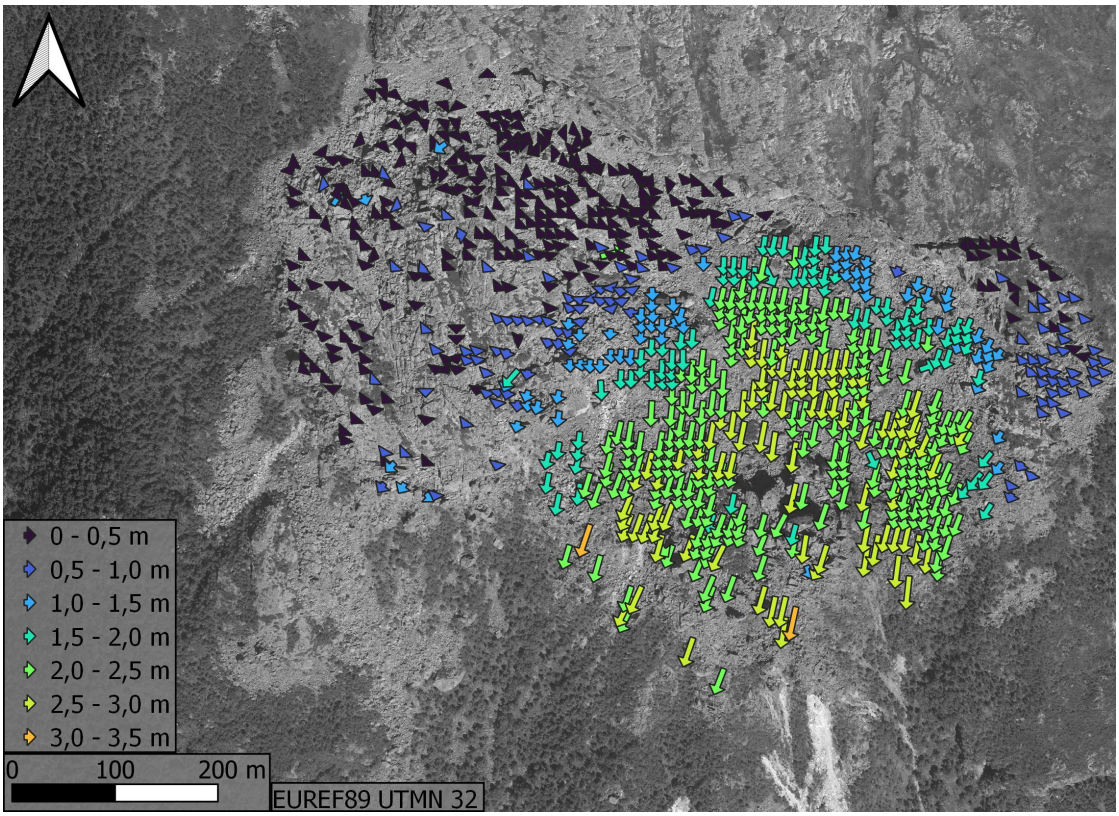

(a) ot1b ot2a

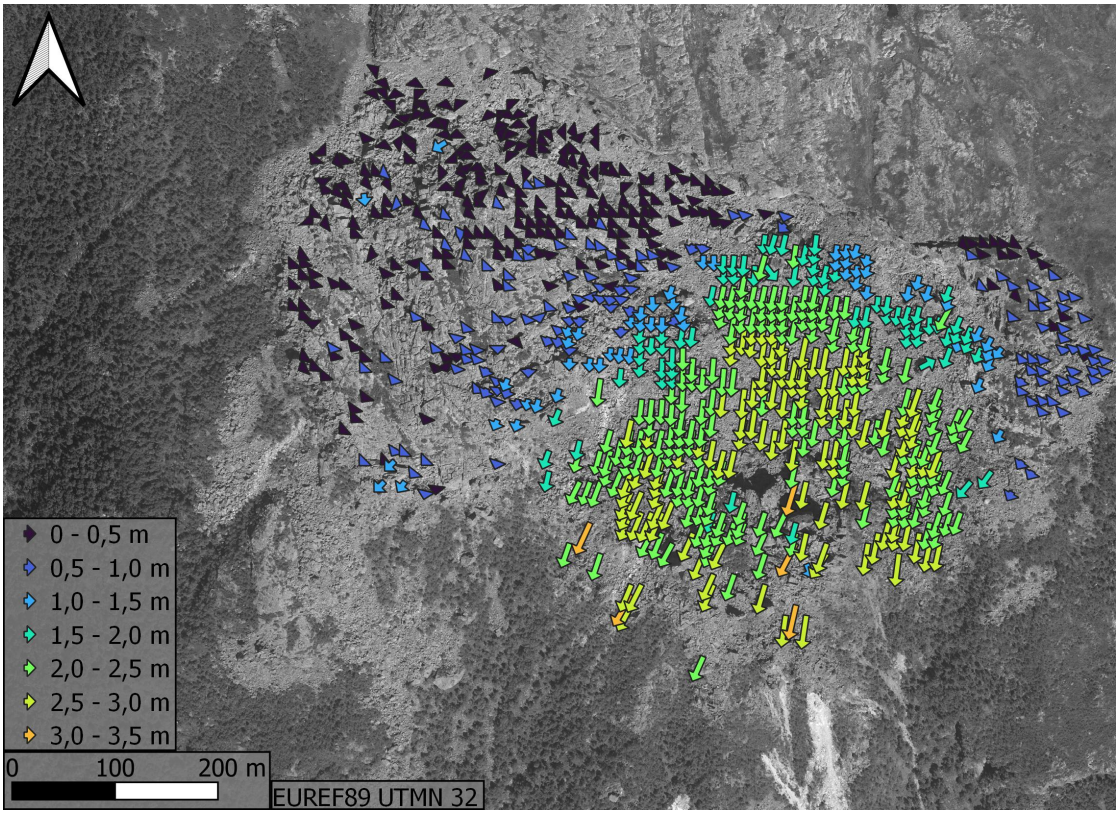

(b) ot1b ot2b

Figure 5.9: Image matching from ot1b to both ot2a and ot2b respectively, where measurements with $\Phi > 0.7$ are filtered out, resulting in 29% in **(a)** and 28% in **(b)** being visible.

Orthomosaics

Displacement vectors found through orthomosaics, either from NIB, or created from the raw images. Figure 5.10 indicates displacement in the upper left section **A** where the vectors are pointing up slope. The single orthoimage results (Figure 5.8, Figure 5.9) indicated movement in a similar direction, Figure 5.10 however, finds displacements of up to 2.5 meters up slope.

Displacement vectors found in Figure 5.11 have a relatively large spread of sizes for both section A and B. Section A ranges from 0 to 5 meters in different areas, which is challenging for determining the actual displacement. Section B has movement ranging predominantly from 3 to 6 meters in the expected down slope direction.

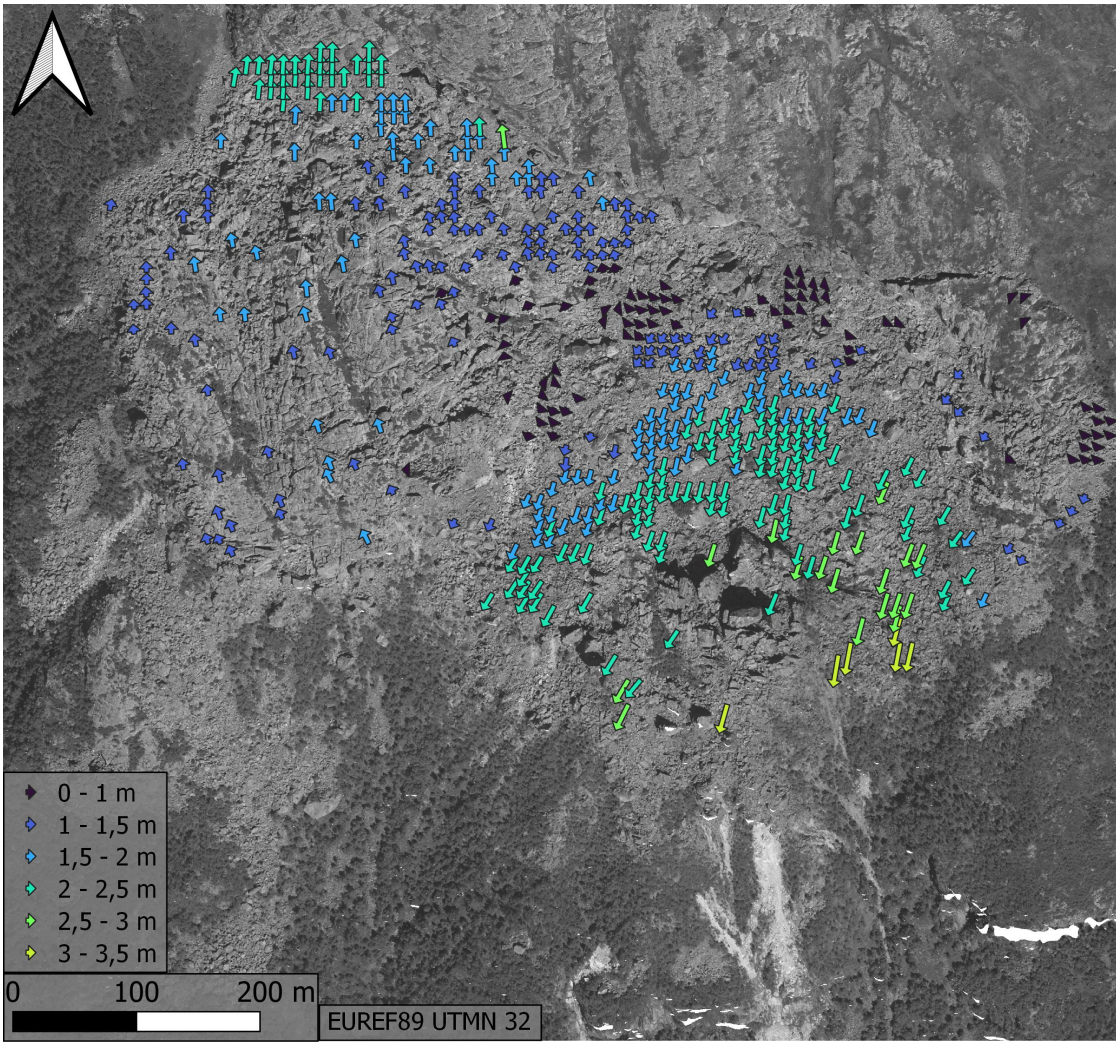

Figure 5.10: Tussafoten orthomosaic displacement vectors between 1969 and 2013, with measurements with $\Phi > 0.7$ filtered out, 32.5% are visible.

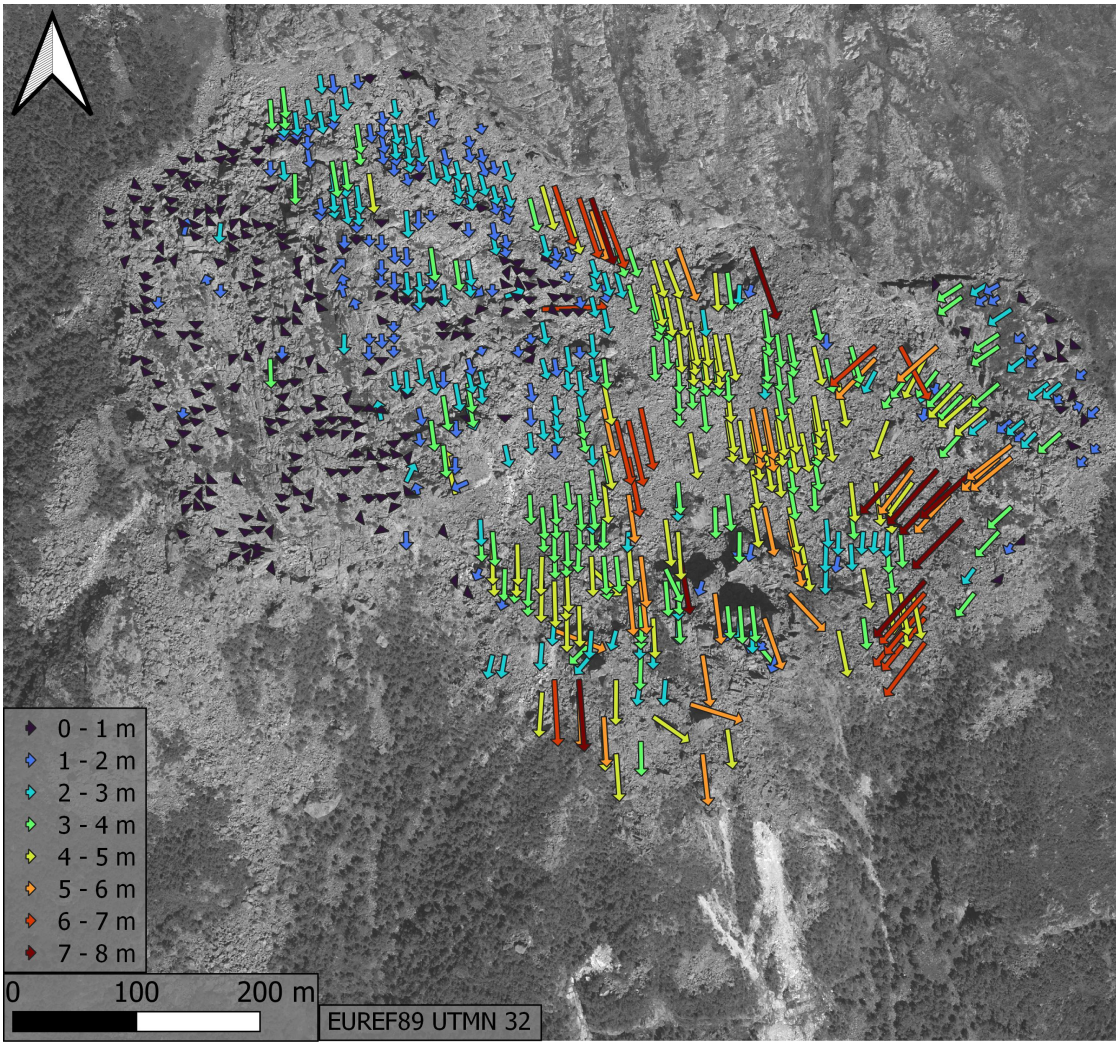

Figure 5.11: Tussafoten displacement vectors between the NIB-images from 1969 and 2013 where measurements with $\Phi > 0.7$ are filtered out, resulting in 25.5% being visible.

5.3.2 Skutshorn

Skutshorn displacements between 2015-2021 from InSAR Norge are found to be: upper section at 2 cmyr^{-1} and lower to be 0,9 cmyr^{-1}, a previous study found an equal velocity in the upper and slightly slower in lower (Pullarello et al. 2021). The difference in time between the time periods of significance (1982-2009 / 1982-2011) is 27 and 29 years which, when averaged out leads to movement of up to 58 cm of the upper section and 26 cm in the lower.

Values of displacements from the NIB images between 1983-2009 (D09) and 1983-2011 (D11) are presented in Table 5.10. Large ranges and high standard deviations are of concern when considering the movement of D11, multiple different filters were attempted and discarded. Displacements of D09 have the lowest σ and more expected movement patterns. The median values of displacements are quite similar for both results, their average speed is between 5,1-5,7 cmyr^{-1}. Considering the direction of movement in Figure 5.12(b) in the upper part of the slide, there is a low possibility of the maximum ranges being correct for D11. The max displacements of the upper part that are travelling in the expected direction reach velocities of 9,8 cmyr^{-1}, though most range between 5-6,7 cmyr^{-1}.

Table 5.10: Displacements occurring at Skutshorn split into the upper and lower part of the ongoing displacement where the upper part is defined as the area above the middle tree-line. **M** is the median, **IQR** is the inter-quantile range, σ is the standard deviation and all results are given in meters.

Images	**M**	**Mean**	**Max**	**Q1**	**Q3**	**IQR**	σ	cmyr^{-1}
				Upper				
1982 - 2009	1,55	1,57	2,65	1,36	1,81	0,45	0,35	5,7
1982 - 2011	1,5	2,24	8,01	0,95	2,38	1,43	2,06	5,3
				Lower				
1982 - 2009	1,14	1,17	2,43	1,05	1,28	0,23	0,19	4,2
1982 - 2011	0,95	1,81	4,23	0,6	2,59	1,99	2,13	3,3

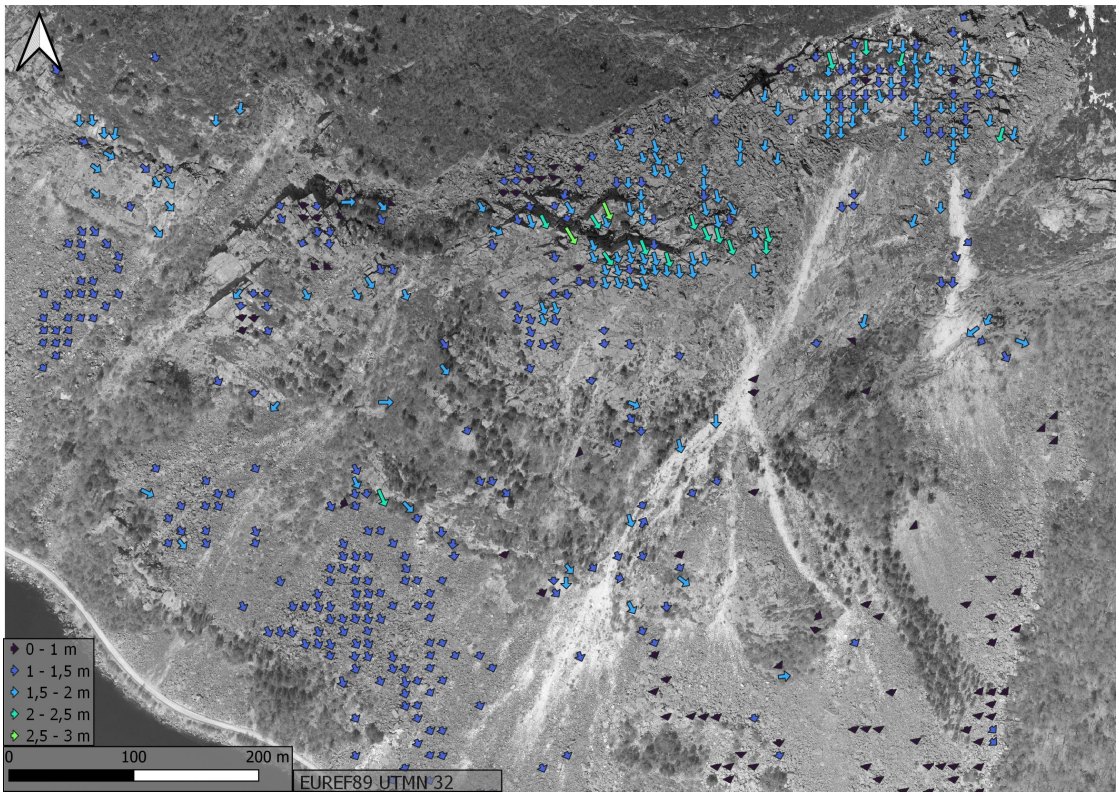

(a) 1982 to 2009

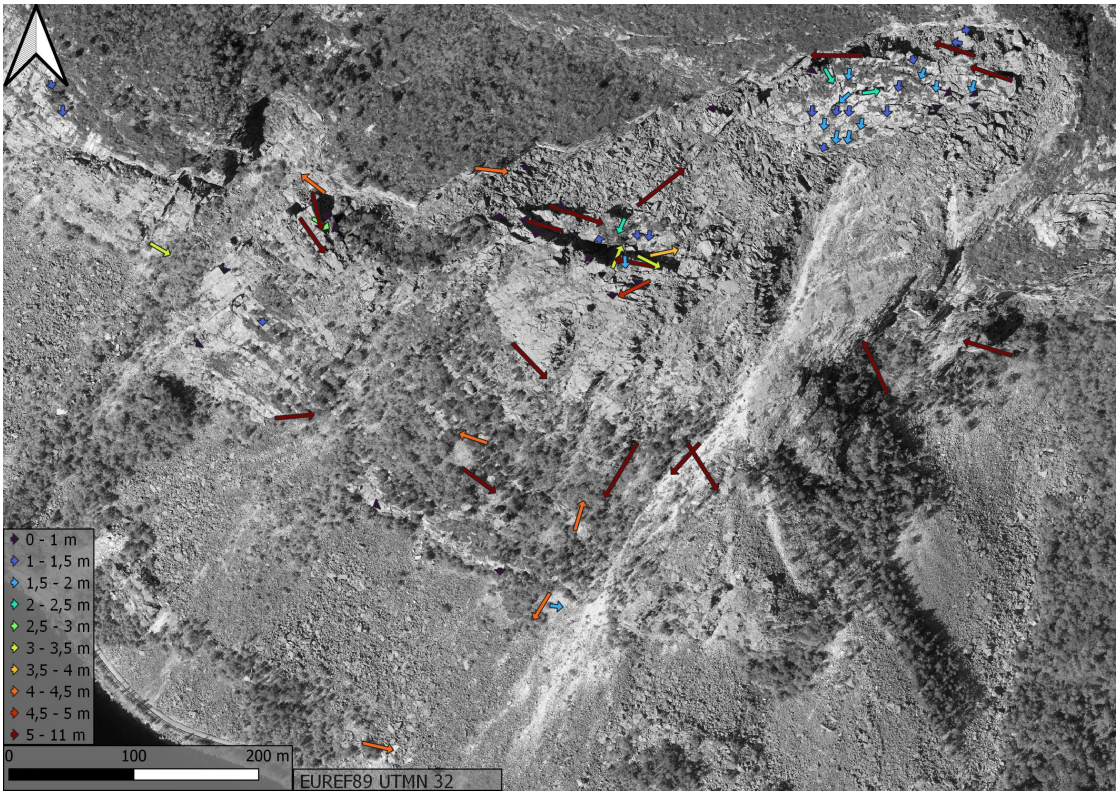

(b) 1982 to 2011

Figure 5.12: Image matching results from Skutshorn filtered with a threshold of $\Phi > 0.7$, leaving 15% visible for **(a)**, and 2% visible for **(b)**.

Chapter 6

Discussion

As per Chapter 1, this study aims to expand temporal data of slow-moving rockslides back in time through analysis of orthorectified images. Techniques used to gather evidence for this study were presented in Chapter 4 and results were presented in Chapter 5. Results included analysis of the images, distortions between images and associated displacement vectors.

The discussion is divided into three parts; analysis and discussion of the orthorectification process and associated accuracy issues, interpretation of the distortions between the images and, finally, attention to the displacement vectors.

6.1 Orthorectification

Deciding to orthorectify images with a more accurate digital elevation model through structure-from-motion was necessary as the Norge I Bilder-images (NIB) use a national 10 m grid digital terrain model (DTM). As mentioned in Section 4.2.1, multiple deviations stemming from the DTM affected the NIB-images negatively. Additionally, the amount of attention to detail for areas in category D is quite low, thus orthorectification with a new digital elevation model (DEM) focusing on the specific area was deemed necessary. The orthorectification process took longer than expected as errors appeared that were not straight-forward to solve. Some uncompressed images had Exif data that indicated they were compressed which was problematic to interpret. While an attempt was made to use the Agisoft Metashape photogrammetric suite, this was discarded as the image quality of the 1969 images were insufficient to identify tiepoints. The images from 2013 were

suitable for defining TPs in Metashape; nonetheless, to avoid confusion only MicMac was used for orthorectification. While a comparison between different photogrammetric suites is not the objective of this study, some insights were gained through this process. As MicMac is an open source highly customizable photogrammetric suite, it requires more experience with photogrammetry than more black-box type suites (Fraser 2013; Griffiths and Burningham 2019; Wackrow and Chandler 2011). This study's "trial and error" attempts with MicMac was quite time consuming for gaining familiarity with the process. The orthorectification process allowed for a better ground sampling distance (GSD) than that was used in this study. A GSD of 0.25 meters was chosen for Tussafoten as that is the same size of the worst quality NIB-image, for sake of comparison.

Computing the absolute orientation was done with a number of ground control points collected from the 2013 NIB-image. These GCPs were often taken from the corner of large elevated objects or from steeper areas and may have propagated into errors (see Figure 2.2). Cost incurred is negligible for more accurate GCPs, which would be to do in situ measurements for increasing the accuracy. Higher accuracy GCPs would warp the images in a more reliable manner during the geometrical correction, which would also affect the resulting digital surface model (DSM). While using the already produced NIB-images for determining displacement between two time periods is the most cost-effective, this study identified various issues.
Errors in position were averaged across the entire orthoimage which likely resulted in a more geometrically correct and accurate orthoimage than the NIB-images. As errors of the GCPs were averaged out instead of more accurate coordinates being averaged out, theoretically this would reduce the absolute accuracy of the images. The values for absolute position as seen in Table 5.1 and Table 5.2, indicate a median uncertainty of 3-4 pixels (0.75-1 m). Furthermore, the Helmert transformations (Table 5.4, Table 5.5) indicate that the shift along the x-, and y-axis is significantly larger between ot1a/b and ot2b than ot2a. The shift that occurs here is possible to mitigate by using the displacements between ot1a or ot1b to ot2a, simply by avoiding ot2b. Although the absolute accuracy acquired is higher than what is expected for NIB-images in the study area, there is still a significant uncertainty. This uncertainty is harder to detect with slow-moving rockslides which may not move enough between the different time periods.

The creation of the DSM resulted in several areas that were challenging for the result

of step 5 from Section 4.1. The slide is located in an area with a gradually increasing slope angle and has a rough surface the steeper the angle of slope, Figure 4.2 shows how some are undefined. As there is an active displacement occurring, the resulting rocks will often rise above the nominal terrain which creates issues with coverage. The resulting "holes" in orthomosaics seen in Figure 5.3(c) indicate a lack of coverage which is more pronounced in the older images. As such areas were patched away by editing the DEM for the NIB-images (Finsrud 2017; Finsrud 2018), they are not easily seen, hence the distortion caused by the editing will be substantial. Orthomosaics created for this study have several "holes" which are unfortunate and can be avoided by using single orthoimages. An argument can thus be made for orthoimages that have not been mosaiced and do not have the resulting holes as seen in (a) and (b) of Figure 5.3.

The images ot1a/b and ot2a/b were taken from the step 5 of Section 4.1. Fortunately the images covered almost the entirety of the slide (Figure 4.4) and it was possible to apply this method by having four images. The area above the slide is relatively flat and has remarkable points in a static feature (rock bed). In hindsight, using a larger amount of GCPs might have increased the absolute accuracy of the DEM and resulting images, although it could also have further warped the images during the geometrical correction.

6.2 Distortions

The orthoimages (Figure 4.4) were taken from an incidence angle that was not attempted to be corrected to a nadir viewpoint. Coverage of objects that are blocked from view are thus difficult to define and some distortions between them were due to the aforementioned angle. Ideally the geometric correction of objects will not be warped significantly between the time periods as they are from slightly different incidence angles. Also, deviations in the DSM from real terrain height leads to horizontal shifts of individual pixels (Kääb and Vollmer 2000).

It is preferable to use stable ground as the baseline for systematic distortion between images, as everything is distortion (Figure 5.5). As Figure 5.3 shows, there are more details in the 2013 images compared to the 1969 images. This results in a varying amount of TPs found, the blurring of the 1969 images likely has a negative effect. On a larger scale in Figure 5.5 for all but (i) and (l), there is a line travelling through the middle from the top of the slide, which is the back scarp. The images from 2013 display higher

quality and less distortion between themselves and the back scarp is not visible as a distortion. Depressions in the rock bed are visible as red distortion "lines" in the middle of the green area, likely due to different incidence angles and or differing vegetation coverage. However, a near vertical line of orange going up next to the green between ot2a/b (Figure 5.5 (i), (l)), remains unexplained.

Triangulating multiple vectors was deemed relevant to determine uncertainties within the orthoimages. Table 5.6 shows uncertainties of similar sizes for all pairs, the differences being at the sub-pixel level make it challenging to determine if any is better than the other. The sum of vectors between orthoimages should, in a perfect world, be equal to zero over stable ground (Table 5.7). While the deviations along the x-axis are significantly larger than for the y-axis, this is possibly due to the location of GCPs. These are predominantly further south in comparison to the stable ground, and are amplified by being collected from the NIB-2013 image which has the inaccuracies of the coarse DEM.

To enhance the validity of the displacements maps the stable ground distortions were used to define an uncertainty. These values are seen in Figure 5.6 where the median value of a stable ground can be defined as systematic distortion. Defining a degree of uncertainty to measurements can help give a clearer picture of the actual displacements that are occurring. Further increasing background information when considering the actual displacements is important for enhanced reliability.

Figure 5.7 indicates that particularly the precision of the orthoimages are higher than the OM or NIB-images. Additionally, the accuracy of the OM is is significantly worse with a median value of roughly 7 pixels. Although the median value of the NIB-image is lower than that of the orthoimages, the spread of the values does indicate there are issues. These distortions suggest that mosaicing images causes effects that are not optimal for the purpose of image matching. Attempts should possibly be made to have data that has the lowest possible amount of distortions over clearly defined stable ground. The results of this study would imply using any of the single orthoimages as they have smaller distortions than what is created through mosaicing.

6.3 Displacement

Knowledge of displacement velocities is a strong indicator of a catastrophic failure, where the average and max velocity are important parameters (Carlà et al. 2019; Federico et al. 2012; Intrieri et al. 2018; Kilburn and Petley 2003; Lacroix, Handwerger and Bièvre 2020). Unknown velocities prior to the discovery of Tussafoten and Skutshorn displacements prompt the question of what is a significantly increasing velocity. The displacement discovered in Section 5.3 can therefore give an idea of an average speed over a longer time-period. The InSAR-data is useful to gain an estimate of potential current displacement. While a heavy caveat with using this data is if the slide is moving faster than the wavelength of the interferometer, which would make this method obsolete. Consequently, this study explores slow-moving rockslides through aerial images taken over a relatively long time period.

6.3.1 Tussafoten

The main objective of this study is to analyze slow-moving rockslide displacements over an extended period of time and give attention to issues that arose in this research process. To uncover what has occurred, several different orthorectified images were used for image matching and are discussed in the following section.

Orthoimages of the slide reveal that displacements are close to what is to be expected from other studies. The issue of interpreting the values becomes challenging as some displacement vectors exist, but they are travelling up slope as seen in Figure 5.8 and Figure 5.9 of section A. This is likely due to the geometrical correction that happened during the orthorectification process. Adding filters would remove this "error", but it is better to have a clearer image of the values that are presented and their distortions. There is also a clear difference in the sum of filtered displacements between Figure 5.8 ot1a-ot2a (a) and ot1a-ot2b (b), likely due to incidence angle and rough topography. The ot1b combinations have overall less displacements filtered out as the image is taken closer to the slide with a (likely) more similar incidence angle. Combined with the results from the Helmert transformation, this suggests that using the values from ot1b-ot2a as being the most accurate.

The displacement lengths, as seen in Table 5.8 suggest that averaged speeds between the time periods are similar to findings in other studies. The maximum velocity found is

between 2,9-4,9 cmyr^{-1}, which goes above the prior velocities, but due to the uncertainty of the images themselves, it is plausible that it has had a steady displacement rate correlated to prior studies. Section B has higher velocities (median of 5,3-5,5 cmyr^{-1} and maximum 6,3-7,6 cmyr^{-1}) which is within the velocities of previous studies, though the averaged InSAR displacement rates (0,8 and 1,9 cmyr^{-1}) are significantly lower. Considering the distortions found over stable ground to be between 3-4 pixels, the velocities are within the expected range of prior studies estimates.

The orthomosaic has multiple displacement vectors travelling up slope in section A (Figure 5.10), rendering the values obsolete. This is likely due to an enhanced effect of what was seen in the orthoimages. Section B of the slide has a larger range of displacements, with velocities between 4,2-7,2 cmyr^{-1}, the spread of displacements are significantly higher than for the orthoimages. Finally, the uncertainty within the orthomosaic is substantial as seen in Figure 5.7, again indicating that orthoimages are preferable.
Although the orthomosaic has the highest median distortion, the spread of distortion for the NIB image is substantial (Figure 5.7), though the median is similar to the orthoimages. The median displacement velocities are the highest of all images for section A and B being at 2 cmyr^{-1} and 8,8 cmyr^{-1} respectively. Furthermore, the maximum velocities being at 27,6 cmyr^{-1} for section A and 25,9 cmyr^{-1} section B are unexpected and likely incorrect. The spread of displacement lengths are large, with the inter-quantile range being significantly larger than others, which makes the NIB challenging to use to define a displacement as its uncertainty is higher than the expected displacement. Stricter thresholds of maximum correlation coefficients do not work in this case, as the maximum displacements found have high maximum correlation coefficient values.

A stricter threshold would lower the amount of displacements which in turn would allow for more accurate displacement values, defining the threshold needs to be done for each independent study.

Large variance in the displacements between the images created in this study and the NIB-images can indicate significant distortion. The terrain is challenging for photogrammetric missions as it is rough, steep and has continuous movement. Defining GCPs with relatively low accuracy during the orthorectification process likely caused the orthoimages and resulting orthomosaic to be warped towards movement travelling up-slope. Avoiding

mosaicing and using purely the orthorectified images is preferable as they have less distortions over stable ground which in turn presents in situ objects correctly. The incidence angle for the images likely has better coverage of section B as the objects in the slide are more visible and well defined than in section A. Although the orthoimages have distortions that are clearly erroneous, the NIB distortion results reveal even larger (most likely) errors that result in uncertain displacement values and is challenging to use for defining prior displacements.

6.3.2 Skutshorn

Displacement vectors from Skutshorn are solely from NIB-orthomosaics, these are values taken at face value with no determination of uncertainty due to lack of stable ground. Below the slide is a small local road before the lake starts, lack of coverage over a larger area with stable non-vegetated ground made it challenging to define a "stable area". Suspected stable areas were suspicious at best as InSAR measurements indicated movement in these locations while the remaining areas are tree-covered which are not suitable for defining uncertainty.
The displacement vectors of Figure 5.12(b) were difficult to define as the 2011 image has bright illumination conditions. Shadows and less contrast made it challenging for image matching to function as shadows are not effected by the normalization process, making the areas look different. While multiple different filters were applied to the displacements vectors, they did however not yield valid results, consequently, it was chosen to visualize the image with the same filter as the rest.

The displacement values between 1982 and 2009 (D09) (Table 5.10) have a lower IQR and σ than the 1982-2011 (D11) displacement results. For D09, the median and averaged displacement velocities are between 5-6,7 cmyr^{-1} which is quite a bit higher than the InSAR results. Skutshorn has active monitoring ongoing, though at the time of this study the data from GNSS measurements has not been released publicly, which would give a better pre-cursor than the InSAR-averaging. The displacement lengths as determined by InSAR do suggest a displacement of 54 cm for the upper part and 24 cm in the lower part for the D09 period. Considering that the displacements lengths from NIB in the Tussafoten slide were likely overestimated, the equally challenging topography of Skutshorn would likely yield many of the same issues.

Chapter 7

Conclusion

The main objective of this study has been to expand temporal data of slow-moving rockslides back in time, determining which method could be suggested and the validity of said results. Orthorectification was conducted to examine which resulting product is best suitable for image matching. Single orthoimages with resulting orthomosaiced images and NIB-images were studied to clarify their resulting distortions when representing a 3D-world in a 2D-image. Conclusions and recommendations from this study are summarised below.

- Structure-from-Motion is a valid method to obtain high quality orthoimages from previous aerial photography missions where insufficient DEMs are used. Orthomosaicing images causes complex distortion patterns that reduce the validity of representing the 3D world and thus reducing the reliability of results from image matching.

- This study evidences that single orthoimages are preferable to orthomosaiced images as they represent the real-world with quantifiable distortions and enable identification of distortion patterns, by measuring displacements of the same and different times allows for selection of reliable displacement combinations. The averaged displacement for Tussafoten between 1969 and 2013 is for section B 4-7 cmyr^{-1} and section A at 1 cmyr^{-1} or lower with an uncertainty over stable ground at 1 m. Reliable combinations are found by applying two methods to interpret displacement vectors, shift along the x-, and y-axis between two images and triangulation of image pairs. In a perfect world, shift along the axis' over stable

ground should be equal to zero; as with triangulation of multiple vectors, these two methods are important for selection of the most reliable displacement fields. Some orthoimages are better than others, and the combinations of matching different pairs enables finding and selecting the optimal pair in terms of least distortion and thus highest displacement accuracy.

- The resulting displacements from NIB images have a high degree of uncertainty, in both study cases the movement has likely been exaggerated. Displacement lengths in the Tussafoten slide extend up to more than 11 m in an area with little expected movement. The NIB-displacements for Skutshorn between 1982 and 2009 seem the least uncertain with an average velocity of 5-7 cmyr^{-1}, though the displacements 1982-2011 are likely erroneous. Furthermore, they use an edited and coarse DEM that pose a challenge which is amplified in rough, steep terrain which is this study's main area of interest. Although they are easily available, they are in some cases too distortend to yield accurate displacements.
- Recommendations: Single-orthoimage processing is recommended as it offers lower degrees of uncertainty and more accurate displacement values. This method can be streamlined by acquiring raw aerial images and in situ visible ground control points on stable ground as in situ investigation with control points is necessary for monitoring unstable rock slopes. With good quality GCPs and stable (preferably) flat ground it is recommended to compute the expected displacements between the respective time periods and a coarser distortion map to determine displacement uncertainties. Consequently, this method requires multiple images that overlap the area of interest and are visible in both time periods without trees and other vegetation that changes and preferably without shadows.

References

Ackermann, F. (1996). 'Techniques and Strategies for DEM Generation'. In: *Digital Photogrammetry*. USA: American Society for Photogrammetry and Remote Sensing.

Azarbayejani, A. and Pentland, A. (1995). 'Recursive estimation of motion, structure, and focal length'. In: *IEEE Transactions on Pattern Analysis and Machine Intelligence* 17, pp. 562–575. DOI: 10.1109/34.387503.

Baltsavias, E. P. (1st Apr. 1996). 'Digital ortho-images — a powerful tool for the extraction of spatial- and geo-information'. In: *ISPRS Journal of Photogrammetry and Remote Sensing* 51.2, pp. 63–77. DOI: 10.1016/0924-2716(95)00014-3.

Bernacki, J. (1st Sept. 2020). 'A survey on digital camera identification methods'. In: *Forensic Science International: Digital Investigation* 34, p. 300983. DOI: 10.1016/j.fsidi.2020.300983.

Carlà, T. et al. (1st Oct. 2019). 'Perspectives on the prediction of catastrophic slope failures from satellite InSAR'. In: *Scientific Reports* 9.1. Number: 1 Publisher: Nature Publishing Group, p. 14137. DOI: 10.1038/s41598-019-50792-y.

Debella-Gilo, M. and Kääb, A. (2012). 'Locally adaptive template sizes for matching repeat images of Earth surface mass movements'. In: *ISPRS Journal of Photogrammetry and Remote Sensing* 69, pp. 10–28. DOI: https://doi.org/10.1016/j.isprsjprs.2012.02.002.

Debella-Gilo, M. and Kääb, A. (17th Jan. 2011). 'Sub-pixel precision image matching for measuring surface displacements on mass movements using normalized cross-correlation'. In: *Remote Sensing of Environment* 115.1, pp. 130–142. DOI: 10.1016/j.rse.2010.08.012.

Eian, R. (2020). - *Hjelper oss å finne ustabile fjellparti*. NGU. URL: https://www.ngu.no/en/node/51052 (visited on 20/01/2023).

Eriksen, H. Ø. et al. (2018). 'Recent Acceleration of a Rock Glacier Complex, Ádjet, Norway, Documented by 62 Years of Remote Sensing Observations'. In: *Geophysical Re-*

search Letters 45.16. _eprint: https://onlinelibrary.wiley.com/doi/pdf/10.1029/2018GL077605, pp. 8314–8323. DOI: 10.1029/2018GL077605.

ESA and IGO, C. B. 3. (2022). *Fucino, Italy*. ESA. URL: https://www.esa.int/ESA_Multimedia/Images/2022/12/Fucino_Italy.

Federico, A. et al. (1st May 2012). 'Prediction of time to slope failure: a general framework'. In: *Environmental Earth Sciences* 66.1, pp. 245–256. DOI: 10.1007/s12665-011-1231-5.

Finsrud, M. (2017). *Ortofoto Rapport Historiske Ortofoto*. NF_0796_ULLENSVANG-1970. Kartverket.

– (2018). *Ortofoto Rapport Historiske Ortofoto NLF-07492 Vang-Slidre 1982*. COWI.

Fraser, C. S. (1st Apr. 2013). 'Automatic Camera Calibration in Close Range Photogrammetry'. In: *Photogrammetric Engineering & Remote Sensing* 79.4, pp. 381–388. DOI: 10.14358/PERS.79.4.381.

Furukawa, Y. and Ponce, J. (Aug. 2010). 'Accurate, Dense, and Robust Multiview Stereopsis'. In: *IEEE Transactions on Pattern Analysis and Machine Intelligence* 32.8. Conference Name: IEEE Transactions on Pattern Analysis and Machine Intelligence, pp. 1362–1376. DOI: 10.1109/TPAMI.2009.161.

Girod, L. (2018). 'Improved measurements of cryospheric processes using advanced photogrammetry'. Accepted: 2018-07-10T14:02:23Z. Doctoral thesis. Universitetet i Oslo.

– (2022). *Introduction to photogrammetry*. University of Oslo.

Glimsdal, S. and Harbitz, C. (2021). *Flodbølger etter skred fra Tussafoten, Eidfjord kommune*. 20210286-01-R. NGI.

– (2022). 'Flodbølger etter skred fra Skutshorn ved Vangsmjøse, Vang kommune'. In: *NVE Rapport nr. 22/2022*.

Griffiths, D. and Burningham, H. (1st Apr. 2019). 'Comparison of pre- and self-calibrated camera calibration models for UAS-derived nadir imagery for a SfM application'. In: *Progress in Physical Geography: Earth and Environment* 43.2. Publisher: SAGE Publications Ltd, pp. 215–235. DOI: 10.1177/0309133318788964.

He, H., Liu, X. and Shen, Y. (1st July 2019). 'Relative radiometric correction of high-resolution remote sensing images based on feature category'. In: *Cluster Computing* 22.4, pp. 7933–7941. DOI: 10.1007/s10586-017-1526-8.

Intrieri, E. et al. (1st Jan. 2018). 'The Maoxian landslide as seen from space: detecting precursors of failure with Sentinel-1 data'. In: *Landslides* 15.1, pp. 123–133. DOI: 10.1007/s10346-017-0915-7.

Jensen, J. J. (1996). 'Confluence of Mapping and Resource Management'. In: *Digital Photogrammetry*. American Society for Photogrammetry and Remote Sensing.

Kääb, A. and Heid, T. (2012). 'Evaluation of existing image matching methods for deriving glacier surface displacements globally from optical satellite imagery'. In: *Remote Sensing of Environment* 118, pp. 339–355. DOI: https://doi.org/10.1016/j.rse.2011.11.024.

Kääb, A., Girod, L. and Berthling, I. (11th June 2014). 'Surface kinematics of periglacial sorted circles using structure-from-motion technology'. In: *The Cryosphere* 8.3. Publisher: Copernicus GmbH, pp. 1041–1056. DOI: 10.5194/tc-8-1041-2014.

Kääb, A. and Vollmer, M. (2000). 'Surface Geometry, Thickness Changes and Flow Fields on Creeping Mountain Permafrost: Automatic Extraction by Digital Image Analysis'. In: *Permafrost and Periglacial Processes* 11.4, pp. 315–326. DOI: 10.1002/1099-1530(200012)11:4<315::AID-PPP365>3.0.CO;2-J.

Kääb, A. (1st Nov. 2002). 'Monitoring high-mountain terrain deformation from repeated air- and spaceborne optical data: examples using digital aerial imagery and ASTER data'. In: *ISPRS Journal of Photogrammetry and Remote Sensing*. Geomatics in Mountainous Areas – The International Year of the Mountains, 2002 57.1, pp. 39–52. DOI: 10.1016/S0924-2716(02)00114-4.

– (2005). *Remote Sensing of Mountain Glaciers and Permafrost Creep*. Schriftenreihe Physische Geographie Glaziologie und Geomorphodynamik. Geographisches Institut der Universität Zürich.

Kartverket and Geovekst-forum (25th Jan. 2020). *Produktspesifikasjon for ortofoto - versjon 5.0*. Kartverket.

Kilburn, C. R. J. and Petley, D. N. (15th Aug. 2003). 'Forecasting giant, catastrophic slope collapse: lessons from Vajont, Northern Italy'. In: *Geomorphology*. Studies on Large Volume Landslides 54.1, pp. 21–32. DOI: 10.1016/S0169-555X(03)00052-7.

Lacroix, P., Handwerger, A. and Bièvre, G. (2020). 'Life and death of slow-moving landslides'. In: *Nature Reviews Earth & Environment* 1, pp. 404–419. DOI: https://doi.org/10.1038/s43017-020-0072-8.

Larsen, L.-H. (8th Apr. 2020). *Vennisvegen blir stengt til over påske*. Avisa Valdres. URL: https://www.avisa-valdres.no/5-54-455065 (visited on 20/01/2023).

Lauknes, T. R. et al. (15th Sept. 2010). 'Detailed rockslide mapping in northern Norway with small baseline and persistent scatterer interferometric SAR time series methods'. In: *Remote Sensing of Environment* 114.9, pp. 2097–2109. DOI: 10.1016/j.rse.2010.04.015.

Lei, Y., Gardner, A. and Agram, P. (Jan. 2021). 'Autonomous Repeat Image Feature Tracking (autoRIFT) and Its Application for Tracking Ice Displacement'. In: *Remote Sensing* 13.4. Number: 4 Publisher: Multidisciplinary Digital Publishing Institute, p. 749. DOI: 10.3390/rs13040749.

Lewis, J. P. (1995). 'Fast normalized cross-correlation'. In: *Vision Interface*. Vision Interface, pp. 120–123.

Linder, W. (2009). *Digital Photogrammetry*. Berlin, Heidelberg: Springer. DOI: 10.1007/978-3-540-92725-9.

Lowe, D. G. (1st Nov. 2004). 'Distinctive Image Features from Scale-Invariant Keypoints'. In: *International Journal of Computer Vision* 60.2, pp. 91–110. DOI: 10.1023/B:VISI.0000029664.99615.94.

Manzer, G. (1996). 'Avoiding Orthophoto Problems'. In: *Digital Photogrammetry*. USA: American Society for Photogrammetry and Remote Sensing.

McNabb, R. (2022). *dem processing using micmac*. iamdonovan. URL: https://iamdonovan.github.io/teaching/egm702/practicals/week1.html.

Messerli, A. and Grinsted, A. (11th Feb. 2015). 'Image georectification and feature tracking toolbox: ImGRAFT'. In: *Geoscientific Instrumentation, Methods and Data Systems* 4.1. Publisher: Copernicus GmbH, pp. 23–34. DOI: 10.5194/gi-4-23-2015.

Nagy, T. et al. (Jan. 2019). 'SenDiT: The Sentinel-2 Displacement Toolbox with Application to Glacier Surface Velocities'. In: *Remote Sensing* 11.10. Number: 10 Publisher: Multidisciplinary Digital Publishing Institute, p. 1151. DOI: 10.3390/rs11101151.

NGU (2022). *Hva er InSAR*. URL: https://www.ngu.no/emne/hva-er-insar (visited on 03/03/2023).

Nicolet, P. and Böhme, M. (2022). *Fare- og risikoklassifisering av det ustabile fjellpartiet Tussafoten i Eidfjord, Vestland*. NGU.

Nicolet, P., Gunleiksrud, I. et al. (2022). *Geologisk modell og fare- og risikoklassifisering av det ustabile fjellpartiet Tussafoten i Eidfjord, Vestland*. 2022.026. NGU.

NVE (2022). *Tussafoten (ustabilt fjellparti)*. URL: https://nve.no/naturfare/overvaking-og-varsling/fjellskredovervaaking/kontinuerlig-overvaakede-fjellpartier/tussafoten/ (visited on 20/01/2023).

PCIGeomatica (25th Nov. 2019). *Geomatica Help*. Version Banff Edition. Ontario, Canada.

Pierrot-Deseilligny, M. (2022). *Documentation MicMac*.

Pollock, W. and Wartman, J. (2020). 'Human Vulnerability to Landslides'. In: *GeoHealth* 4.10. DOI: https://doi.org/10.1029/2020GH000287.

Pullarello, J. et al. (2021). 'First results from the Skutshorn rock slope instability, Vang Municipality, Innlandet'. In: *Abstracts and Proceedings of the geological society of Norway* 1, p. 62.

Reit, B.-G. (2009). *On geodetic transformations*. LMV-rapport 2010:1. Gävle: Lantmäteriet, p. 57.

Rexer, M. and Hirt, C. (2014). 'Comparison of free high resolution digital elevation data sets (ASTER GDEM2, SRTM v2.1/v4.1) and validation against accurate heights from the Australian National Gravity Database'. In: *Australian Jorunal of Earth Sciences* 61.2, pp. 213–226. DOI: https://doi.org/10.1080/08120099.2014.884983.

Rupnik, E., Daakir, M. and Pierrot Deseilligny, M. (5th June 2017). 'MicMac – a free, open-source solution for photogrammetry'. In: *Open Geospatial Data, Software and Standards* 2.1, p. 14. DOI: 10.1186/s40965-017-0027-2.

Rupnik, E., Deseilligny, M. P. et al. (2016). 'Refined satellite image orientation in the free open-source photogrammetric tools apero/micmac'. In: *ISPRS Journal of Photogrammetry and Remote Sensing* III-1.

Scambos, T. A. et al. (1st Dec. 1992). 'Application of image cross-correlation to the measurement of glacier velocity using satellite image data'. In: *Remote Sensing of Environment* 42.3, pp. 177–186. DOI: 10.1016/0034-4257(92)90101-O.

Schenk, T. (1999). *Digital Photogrammetry: vol. i : background, fundamentals, automatic orientation procedures*. TerraScience.

Skistad, K. (2014). *Omløpsfotografering Hardangervidda 2013*. LOMK0002. TerraTec.

Snavely, K. N. (2008). 'Scene Reconstruction and Visualization from Internet Photo Collections'. PhD thesis. University of Washington.

Vogt, L. F. and Nordrum, I. A. (2017). '"Kjør" nye E16 over Filefjell'. In: *NRK*.

Wackrow, R. and Chandler, J. H. (2011). 'Minimising systematic error surfaces in digital elevation models using oblique convergent imagery'. In: *The Photogrammetric*

Record 26.133. _eprint: https://onlinelibrary.wiley.com/doi/pdf/10.1111/j.1477-9730.2011.00623.x, pp. 16–31. DOI: 10.1111/j.1477-9730.2011.00623.x.

Wasowski, J. and Bovenga, F. (23rd May 2014). 'Investigating landslides and unstable slopes with satellite Multi Temporal Interferometry: Current issues and future perspectives'. In: *Engineering Geology* 174, pp. 103–138. DOI: 10.1016/j.enggeo.2014.03.003.

Watson, G. A. (15th Dec. 2006). 'Computing Helmert transformations'. In: *Journal of Computational and Applied Mathematics* 197.2, pp. 387–394. DOI: 10.1016/j.cam.2005.06.047.

Westoby, M. et al. (2012). ''Structure-from-Motion' photogrammetry: A low-cost, effective tool for geoscience applications - ScienceDirect'. In: *Geomorphology* 179, pp. 300–314. DOI: https://doi.org/10.1016/j.geomorph.2012.08.021.